Applied Scanning Probe Methods Vol. XI, eds. B. Bhushan and H. Fuchs
(Springer-Verlag, Berlin Heidelberg New York, 2009), Chapter 5, pp. 97-138
The original publication is available at http://www.springerlink.com
Some figures have been changed to color from the original black and white.

Contact Resonance Force Microscopy Techniques for Nanomechanical Measurements*

D. C. Hurley
National Institute of Standards & Technology
325 Broadway
Boulder, Colorado 80305 USA
email: hurley@boulder.nist.gov
tel: +1-303-497-3081

Contact resonance force microscopy (CR-FM) methods such as atomic force acoustic microscopy show great promise as tools for nanoscale materials research. However, accurate and reliable CR-FM measurements require the simultaneous optimization of a large number of experimental conditions. Among these variables are cantilever spring constant, applied static load, reference material, and resonant mode (mode type and order). In addition, results depend on the models used for data analysis and interpretation (*e.g.*, choice of contact-mechanics model). All of these parameters are linked in numerous ways that are not straightforward to classify. In this chapter, we present a "user's guide" to quantitative measurements of nanomechanical properties with CR-FM methods. The discussion emphasizes the experimental methods and their practical implementation, providing a snapshot of the current state of the art. We discuss the basic physical principles involved and show how they can be used to make informed choices about experimental parameters and operating conditions. Experimental data and the results of theoretical models are provided as specific examples of the abstract concepts. Ideas for future work are also discussed, including ways to simplify the measurement process or improve measurement accuracy. The objective is not only to enable readers to perform their own CR-FM measurements, but also to optimize experimental conditions for a given material system. By gaining a better understanding of the underlying measurement principles, more researchers will be encouraged to further extend the technique and use it for an ever-wider range of applications for the nanoscale characterization of materials.

keywords: atomic force acoustic microscopy (AFAM), contact resonance force microscopy (CR-FM), elastic properties, nanomechanical properties

Abbreviations

a	Contact radius between the tip and the sample
α	Tilt angle of the cantilever
b	Thickness of the cantilever
β	Exponent to describe the dependence of contact stiffness on applied force
c_B	Characteristic parameter of the cantilever
d	Deflection of the cantilever
d_0	"Jump to contact" deflection of the cantilever
E	Young's modulus
E^*	Reduced elastic modulus
F_N	Static force applied normal to the surface by the tip
f_n	Contact-resonance frequency of the nth flexural mode
f_n^0	Natural (free) frequency of the nth flexural mode
γ	Relative position of the cantilever tip
h	Height of the tip
k_{lever}	Flexural stiffness or spring constant of the cantilever
k, κ	Normal, lateral contact stiffness
L	Length of the cantilever
L_1	Distance from the fixed end of the cantilever to the tip
L'	Distance from the free end of the cantilever to the tip
M	Indentation (plane strain) modulus
m	Exponent to describe the tip-sample contact
n	Mode number
ν	Poisson's ratio
p_0	Normal component of the compressional stress applied at the sample surface by the tip
R	Radius of curvature of the tip
r	Radial distance from the axis of the tip
ρ	Mass density
S	Sensitivity of the mode response; derivative of the frequency versus contact stiffness curve
s	Sensitivity of the cantilever
σ_r	Radial component of the tensile stress in the sample
σ_z	Normal component of the compressional stress in the sample beneath the axis of the tip
w	Width of the cantilever
x_n^0	Wavenumber of the nth flexural free resonance
z	Normal depth from the surface of the sample

AFM	Atomic force microscopy
AFAM	Atomic force acoustic microscopy
CR-FM	Contact resonance force microscopy
NI	Instrumented (nano-) indentation
SAWS	Surface acoustic wave spectroscopy
UAFM	Ultrasonic AFM
UFM	Ultrasonic force microscopy

1 Introduction

"The ability to accurately and reproducibly measure the properties and performance characteristics of nanoscale materials, devices, and systems is a critical enabler for progress in fundamental nanoscience, in the design of new nanomaterials, and ultimately in manufacturing new nanoscale products [1]." This quotation from the US National Nanotechnology Initiative emphasizes the need for measurement tools in emerging nanomaterial applications, a field predicted to generate a multibillion-dollar market within 10 years. One specific measurement need is for nanomechanical information—knowledge on the nanoscale of mechanical properties such as elastic modulus, adhesion, and friction. Accurate information is essential not only to predict the performance of a system before use, but also to evaluate its reliability during or after use. The measurement need is motivated partly by the fact that new applications often involve structures with nanoscale dimensions (*e.g.*, nanoelectromechanical systems, nanoimprint lithography). Measurements of such structures by necessity must provide nanoscale spatial resolution. Other new structures have larger overall dimensions, but integrate disparate materials on the micro- or nanoscale (*e.g.*, electronic interconnect, nanocomposites). In such cases, nanoscale information is needed in order to differentiate the properties of the various components.

Many methods to measure small-scale mechanical properties have been devised, including ones based on indentation [2-4], on ultrasonics [5,6], and on other physical phenomena [7,8]. Such methods often have drawbacks: they are not sufficiently quantitative, are limited to specialized geometries, and so forth. For instance, instrumented or "nano-" indentation (NI) [2] is inherently destructive, creating indents hundreds to thousands of nanometers wide. Conventional NI techniques may also provide insufficient spatial resolution as dimensions shrink further. A promising approach combines low-load NI techniques with force modulation and scanning [3]. However, the lateral resolution is still restricted by the radius (a few hundred nanometers) of the Berkovich diamond indenter employed.

Atomic force microscopy (AFM) methods present an attractive alternative for measuring mechanical properties. The small radius of the cantilever tip (~5 nm to 50 nm) provides nanoscale spatial resolution. Furthermore, the scanning capability of the AFM instrument enables rapid, in-situ imaging. AFM was originally developed to measure surface topography with atomic spatial resolution [9]. Since then, several AFM techniques have been demonstrated to sense mechanical properties [10-13]. Methods to measure mechanical properties that are based on force-displacement curves have also been extensively developed (see Ref. [14] for a review). Force-displacement methods work best when the compliance of the cantilever is roughly comparable to that of the test material. Therefore, these methods are better suited to very compliant ("soft") materials, and lose effectiveness as the material stiffness increases. The most promising AFM methods for quantitative measurements of relatively stiff materials such as ceramics or metals are dynamic approaches in which the cantilever is vibrated at or near its resonant frequencies [15]. These methods are often labeled "acoustic" or "ultrasonic", due to the frequency of vibration involved (~100 kHz to 3 MHz). Among them are ultrasonic force microscopy (UFM) [16,17], heterodyne force microscopy [18], ultrasonic atomic force microscopy (UAFM) [19] and atomic force acoustic microscopy (AFAM) [20].

Of these methods, AFAM (and to a lesser extent, UAFM) has achieved the most progress in quantitative measurements. A general name for approaches such as AFAM and UAFM is "contact resonance spectroscopy AFM" or more simply "contact resonance force microscopy" (CR-FM). The key concepts of CR-FM are illustrated in Fig. 1.1. Resonant vibrational modes of the cantilever are excited either by an external actuator, as shown in the figure, or by an actuator attached to the AFM cantilever holder. When the tip of the cantilever is out of contact with the sample [Fig. 1.1(a)], the resonant modes occur at specific frequencies that depend on the geometry and material properties of the cantilever. When the tip is placed in contact [Fig. 1.1(b)], the frequencies of the resonant modes increase due to tip-sample forces [Fig. 1.1(c)]. CR-FM involves measuring the frequencies at which the free and contact resonances occur. The mechanical properties of the sample are then deduced from these frequencies with the help of appropriate models. Quantitative measurements have also been demonstrated with UFM methods [21].

Fig. 1.1 Concepts of contact resonance force microscopy (CR-FM). Resonant modes of the cantilever are excited by a piezoelectric actuator when the tip is (a) in free space and (b) in contact with a specimen under an applied static force. (c) Resonant spectra. The lowest-order contact resonance occurs at a higher frequency than the first free-space resonance, but is lower than the second free-space resonance.

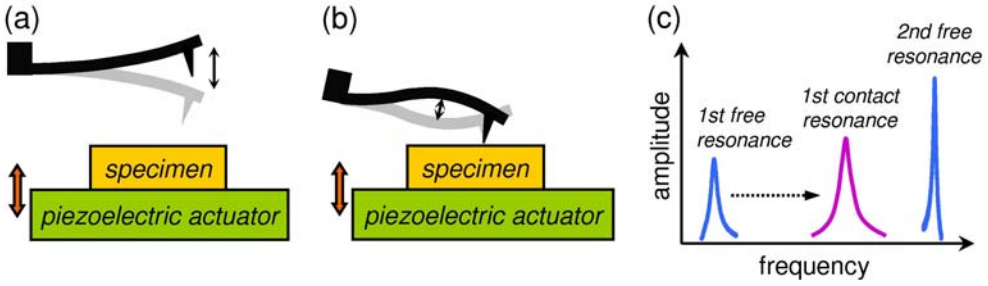

In this chapter, we present a "user's guide" to quantitative measurements of nanomechanical properties with CR-FM methods. An earlier chapter in this series by Rabe [22] provided a comprehensive review focusing on the technique's theoretical foundation. Here, the discussion emphasizes the experimental methods and their practical implementation, providing a snapshot of the state of the art. Current best practices for data acquisition and analysis are not merely stated, but are explained and justified in terms of the physical principles involved. Practical examples are provided to illustrate the concepts discussed. Our objective is to enable readers not only to perform CR-FM measurements, but also to optimize experimental conditions for their particular needs. By gaining a better understanding of the underlying measurement principles, more researchers will be encouraged to further extend the technique and use it for an ever-wider range of applications.

2 Cantilevers for Contact Resonance Force Microscopy

Accurate CR-FM measurements begin by choosing a suitable cantilever. Measurements on stiff materials (modulus greater than approximately 50 GPa) involve relatively stiff cantilevers—ones with a spring constant k_{lever} of approximately 30 N/m to

50 N/m. A variety of such cantilevers are available commercially and are usually sold as "noncontact" or "intermittent contact" probes. As seen below, interpretation of CR-FM data requires a model for the vibrating cantilever. The model assumes that the cantilever is a uniform rectangular beam, so that analytical expressions can be derived. For this reason, the cantilevers typically used in CR-FM have a simple rectangular shape and are micromachined from single-crystal silicon (Si). The long axis of the cantilever is oriented in the <110> crystalline direction, and the axis of the tip is <001>-oriented.

Table 2.1 Properties of cantilevers used in CR-FM experiments. Shown are the nominal length L, width w, thickness b, and nominal spring constant k_{lever} cited by the manufacturer. Also given are the measured values of the four lowest free resonant frequencies and the frequency ratio f_n^0/f_1^0 of the nth free frequency to the first free frequency. f_4^0 could not be measured for cantilevers #1 and #2 due to bandwidth limitations of the AFM photodiode. The "theory" column shows the values of f_n^0/f_1^0 predicted by the analytical model discussed in the text.

property	**cantilever #**				**theory**
	1	**2**	**3**	**4**	
L (μm)	225	230	230	450	
w (μm)	38	40	40	55	
b (μm)	7	7	3	4	
k_{lever} (N/m)	48	40	3.5	1.6	
f_1^0 (kHz)	171.66	167.68	72.76	20.99	
f_2^0 (kHz)	1066.5	1071.2	501.57	131.40	
f_3^0 (kHz)	2937.3	3011.7	1464.2	368.24	
f_4^0 (kHz)	—	—	2956.4	721.09	
f_2^0/f_1^0	6.21	6.39	6.89	6.26	6.27
f_3^0/f_1^0	17.11	17.96	20.12	17.54	17.55
f_4^0/f_1^0	—	—	40.63	34.35	34.39

Table 2.1 contains information about several AFM cantilevers. The table shows the nominal length L, width w, thickness b, and spring constant k_{lever} for each cantilever, as given by the manufacturer. For a simple rectangular cantilever beam, k_{lever} may be determined from the relationship $k_{lever} = Eb^3w/(4L^3)$, where E is Young's modulus. The table also gives measured values of the frequency f_n^0 of the nth order flexural free resonance for each cantilever. Cantilever #1 is the type most frequently used for CR-FM experiments in our laboratory. Cantilever #2 has dimensions and spring constant similar to those of #1, but was made by a different manufacturer. Note that these cantilevers are relatively long. Shorter cantilevers with similar values of k_{lever} are available (*e.g.*, $L \approx 125$ μm), but their resonant frequencies will be higher and could be difficult to detect, given the finite bandwidth of the AFM photodiode detector. Cantilever #3 is similar to #1 and

#2 in length and width, but is thinner and therefore has a lower k_{lever}. The spring constant of cantilever #4 is even lower, because it is thinner and longer.

To perform measurements, cantilevers are mounted in the standard holder provided by the AFM manufacturer. Recent research indicates that the mounting or clamping conditions of the cantilever in the holder can affect the measurements in some cases [23]. Depending on the specific holder used, it may therefore be advisable to develop an improved mounting method (*e.g.*, gluing the cantilever in the holder, using a firmer clamp). Further work is needed to better understand the practical implications of these effects on measurements.

Before performing contact experiments, the cantilever's free (natural) frequencies when the tip is out of contact must be measured. The values of the free frequencies are used to characterize the cantilever's properties, as discussed below. Typically, the free frequencies f_n^0 of the lowest two or three flexural modes are measured. One way to measure the free frequencies is with the AFM's "tuning" software intended for intermittent-contact operation. The subroutine controls a small piezoelectric actuator at the clamped end of the cantilever. Depending on the frequency characteristics of the actuator, however, it may be difficult to excite the higher-order modes in this way. Alternatively, the free frequencies can be measured with a piezoelectric actuator mounted beneath the specimen. The cantilever is brought close to, but not in contact with, the specimen. Driving the actuator at relatively high voltages creates acoustic vibrations that are large enough to excite the cantilever's free resonances via air coupling. Measured values of f_n^0 for cantilevers #1-#4 are given in Table 2.1.

Determining the free frequencies is necessary for data analysis, but also serves a second purpose. The ratio f_n^0/f_1^0 of the nth free mode to the lowest mode f_1^0 is an indicator of measurement quality. The closer the measured values of f_n^0/f_1^0 are to those predicted by the analytical model, the more likely it is that the model accurately describes the dynamics of the actual cantilever. Table 2.1 contains the measured ratios f_n^0/f_1^0 for the four cantilevers. The predicted and measured ratios differ by less than 3 % for #1 and #2, and less than 0.2 % for #4. The discrepancies are probably due to small variations in the micromachining process, for instance small irregularities in the cross section or a thickness variation along the length of the cantilever [24]. In the case of cantilever #3, the measured and predicted values of f_n^0/f_1^0 differ by more than 10 %. Use of such cantilevers should be avoided if possible. One possible explanation for the discrepancy is that the top side of cantilever #3 contains a thin reflective film to boost the detected signal amplitude. In practice, we are able to achieve adequate signal amplitude with uncoated cantilevers.

The scanning electron microscope (SEM) can be used to obtain additional information about cantilevers. Figure 2.1 shows SEM images of two cantilevers that are candidates for CR-FM experiments. Figures 2.1(a)-(c) were acquired with a cantilever similar to #1 in Table 2.1, while Figs. 2.1(d)-(f) were acquired with cantilever #2. Several observations can be made from the images. First, the cross section of each cantilever is actually trapezoidal, not rectangular. This is more pronounced in the first cantilever. The cross section is uniform throughout most of the length of the cantilever, but varies in both width and thickness at the very end of the cantilever. In addition, the tip is not located at the very end of the cantilever. The distance between the tip and the end of the cantilever differs from cantilever to cantilever. Finally, the tip of cantilever #2 is noticeably longer.

Fig. 2.1 SEM images of single-crystal silicon cantilevers. (a) Plan view of the underside of a cantilever similar to #1 in Table 2.1. (b) Side view and (c) plan view of the tip end of the cantilever. (d) Closeup of the tip end of cantilever #2 in Table 2.1. (e) Plan view of the underside of cantilever #2. (f) Side view of the tip end of the cantilever.

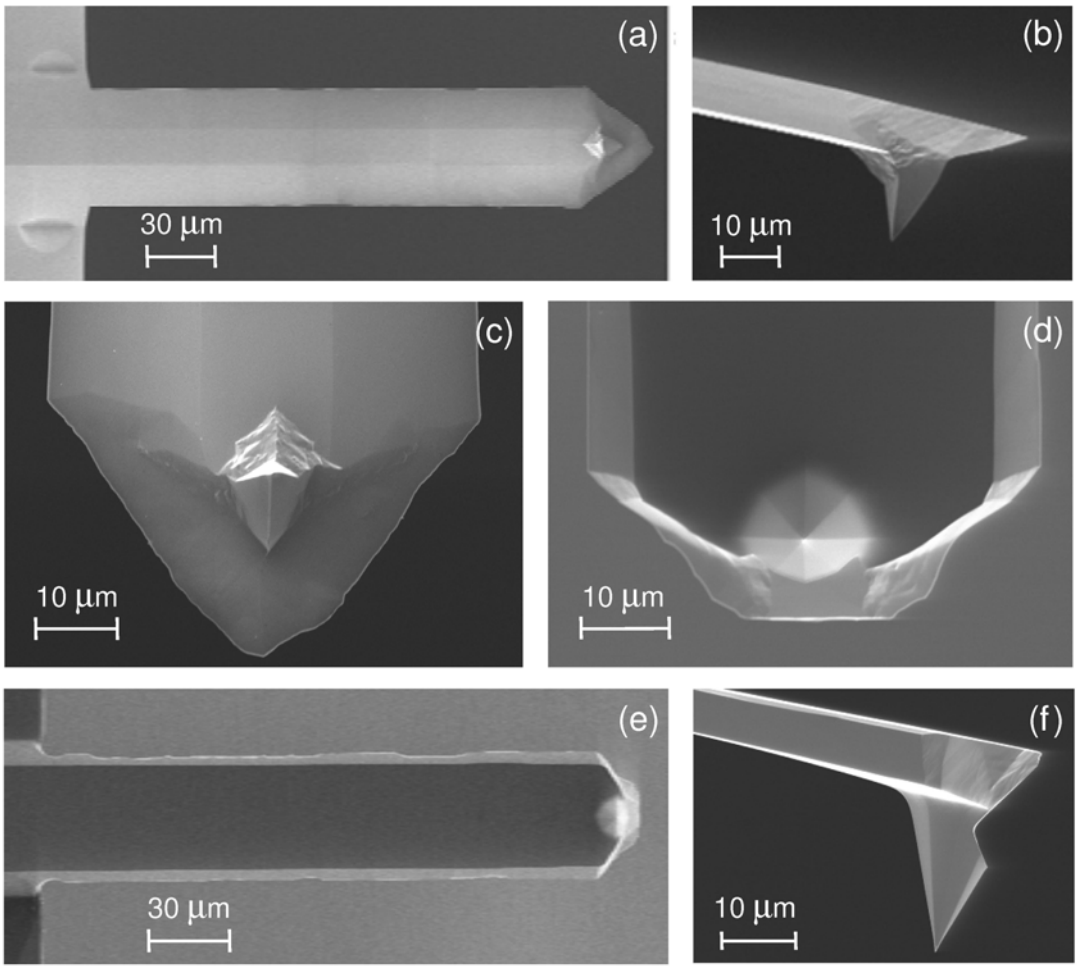

3 Data Acquisition Techniques

In this section, we describe current practices for quantitative measurements of elastic modulus with CR-FM. A "recipe" is presented based on standard practices of our own and other groups. Following this recipe will enable readers to perform similar measurements themselves. Familiarity with the recipe is also necessary to understand subsequent discussions about improving and optimizing measurements.

Figure 3.1 shows a block diagram of the apparatus used in our laboratory for CR-FM experiments. The constituent components, all of which are commercially available, include (a) an AFM instrument, (b) a function generator and piezoelectric actuator to excite the cantilever resonances, (c) a lock-in amplifier for frequency-selective signal detection, and (d) a computer for instrument control and data acquisition. The equipment used in our laboratory is specified here, but other equipment with similar characteristics could also be used [25].

Contact-resonance experiments have been performed with several different AFM instruments, including the Digital Instruments Dimension 3000 (Veeco Metrology, Inc., Santa Barbara, CA) and the Asylum MFP-3D (Asylum Research, Santa Barbara, CA). The AFM instrument must meet two main requirements. First, it must provide access to the unfiltered, high-frequency photodiode detector signal. Second, the bandwidth of this signal must be sufficient to detect frequencies up to at least 2 MHz (preferably 3 MHz). Access is provided in some instruments by an accessory unit. The ability to input an external signal for image acquisition is also useful, although not strictly required for modulus measurements.

Fig. 3.1 Block diagram of apparatus for CR-FM experiments.

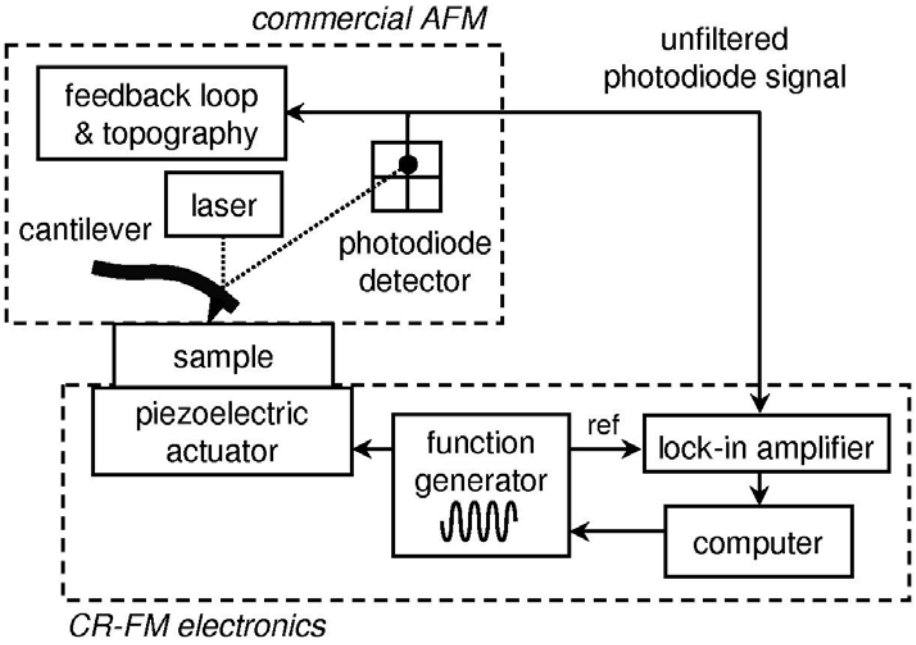

As a piezoelectric actuator, we find it convenient to use ultrasonic contact transducers designed for nondestructive testing (Panametrics, Olympus NDT, Waltham, MA). Longitudinal transducers with the excitation motion normal to the transducer surface are suitable for experiments involving flexural modes. The piezoelectric element in these transducers is heavily damped for a broad frequency response (typically, –6 dB rolloff at ±50 % of the center frequency). Thus, a single transducer with a center frequency of 1 MHz or 2.25 MHz can excite all of the cantilever resonances from approximately 100 kHz to 3 MHz. Another advantage of these transducers is their relatively large diameter (approximately 1 cm to 3 cm). This means that reasonably large specimens can be accommodated, and that the vibration amplitude varies fairly slowly across the specimen. The simplest way to mount the sample is to bond it directly to the top of the transducer. Various glues provide a rigid bond, but sample removal is easier if an acoustic couplant such as glycerin is used. Samples mounted in this way should be allowed to "settle" for several hours or overnight to ensure stable measurements.

The piezoelectric transducer is driven with a continuous sine wave signal from a function generator (33120A, Agilent Technologies, Santa Clara, CA). The primary requirements are a programmable output with adjustable frequency (~10 kHz to 3 MHz) and amplitude (0 V to 5 V peak-to-peak). The required voltage amplitude depends on the actuator used. The actuator vibration must be sufficiently strong to excite the resonant modes of the cantilever when the tip is in contact, yet the vibration amplitude must be sufficiently small that the tip and the sample remain in contact at all times. Continuous contact ensures a linear elastic regime, so that the assumptions of the data analysis model are valid. With the transducers described above, a driving amplitude of approximately 100 mV or less is usually adequate. Optical measurements with a Michelson interferometer on similar transducers suggest that the peak vibration amplitude at the surface of the transducer is much less than 0.1 nm at this level of excitation voltage.

The photodiode detector signal from the AFM instrument is connected to the input of a lock-in amplifier (SR844, Stanford Research Systems, Sunnyvale, CA). The lock-in must have sufficient bandwidth to detect the contact-resonance frequencies. The sync signal from the function generator provides the reference signal for the lock-in amplifier. With this arrangement, the output amplitude of the lock-in gives the amplitude of cantilever vibration only at the excitation frequency.

Data acquisition software is straightforward and can be created with commercial tools such as LabVIEW (National Instruments Corp., Austin, TX). In the data acquisition routine, the function generator is programmed to output a continuous sine wave with a specific frequency and amplitude. The resulting output signal of the lock-in amplifier is then recorded. The excitation frequency is incrementally increased, and the sequence is repeated until the desired maximum frequency is reached. In this way, a spectrum of the cantilever vibration amplitude versus frequency is recorded. Both the amplitude and phase of the lock-in amplifier signal are recorded. To date, the phase information has not been formally used in the data analysis. However, it can be useful in identifying the exact resonant frequency if the amplitude peak is very small.

Examples of experimental contact-resonance spectra are shown in Fig. 3.2. The data were acquired with cantilever #1 in Table 2.1. Spectra of the first, second, and third free-space flexural resonances are shown in Figs. 3.2(a), (c), and (e), respectively. The corresponding contact-resonance spectra are shown in Figs. 3.2(b), (d), and (f). The sample was a <102> SnO_2 nanobelt [26]. Spectra are shown for two values of the static cantilever deflection d. Using the relation $F_N = k_{lever}\, d$ between the deflection d and the resulting static force F_N and assuming k_{lever} = 48 N/m, it is found that F_N = 0.7 μN and 2.2 μN for d = 15 nm (dashed line) and d = 45 nm (solid line). The spectra show that the peak contact-resonance frequency increases with increasing F_N (or d). As discussed below, such behavior is predicted by the contact mechanics models used for data analysis. The amplitude of the signal also tends to increase with increasing F_N, although this is not always true. The signal amplitude can be seen to decrease with increasing mode number or frequency. One explanation for this trend could be rolloff in the frequency response of the AFM photodiode detector.

CR-FM experiments consist of acquiring contact-resonance spectra for two specimens in alternation: the “test” (unknown) specimen and a “reference” specimen whose elastic properties are known. Reasons for this referencing approach are discussed below in Sec. 4. The elastic properties of reference specimens can be determined by

various means, including pulse-echo ultrasonics [27] and instrumented (nano-) indentation [2,28]. For accurate measurements, the elastic properties of the reference specimen should be similar to those of the test specimen [24,29,30]. If possible, a means to measure both specimens at the same time should be devised in order to avoid repeated mounting and unmounting. It is important that the alignment of the laser spot on the cantilever remains the same throughout all of the measurements. This ensures that measurements made at the same static deflection d correspond to the same static load F_N, without direct measurement of the spring constant k_{lever}.

Fig. 3.2 Examples of experimental results. (a), (c), and (e): Spectra of the first, second, and third free-space flexural resonances. (b), (d), (f): Corresponding contact-resonance spectra for d = 15 nm (dashed line) and d = 45 nm (solid line).

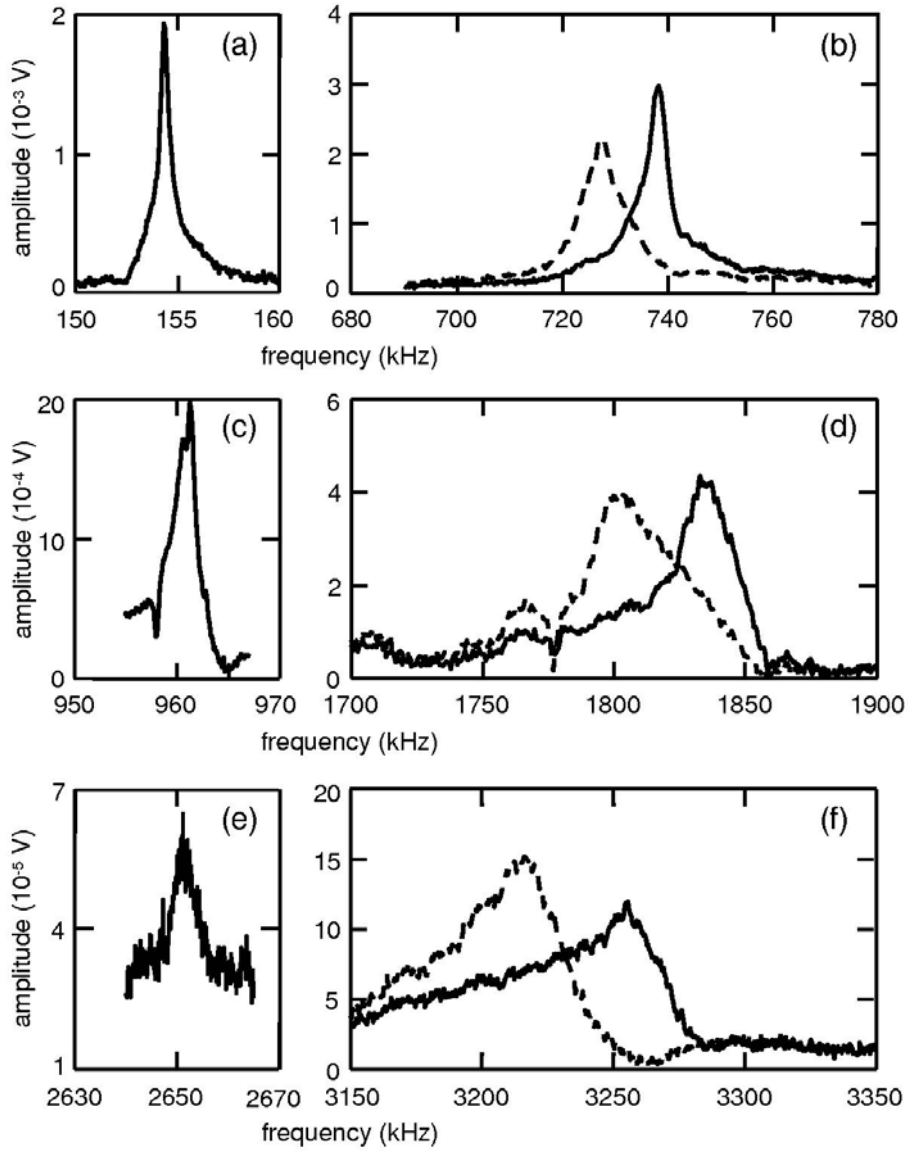

The basic measurement procedure consists of the following steps:

1. Measure the free frequencies f_n^0 of the two lowest flexural modes.

2. Bring the cantilever into contact with the reference specimen. The tip must remain stationary (i.e., set the scan size to zero).

3. Acquire force-distance ("force calibration") curves to determine the cantilever sensitivity ("optical lever sensitivity"). The sensitivity s relates the deflection d of the cantilever to the output voltage of the photodiode detector. Thus if s = 100 nm/V, increasing the setpoint voltage by 0.1 V will increase d by 10 nm. Also note the "pull-on" or "jump to contact" deflection d_0, which indicates the adhesion.

4. Set the static deflection d of the cantilever to a specific value. Typically, d ranges from 10 nm to 60 nm. Elastic contact between the tip and the sample is needed to ensure that the analysis model is valid. Therefore d should be at least ten times larger than the deflection d_0 due to adhesion. However, d should be kept as low as possible to minimize potential damage to both the tip and the sample.

5. Acquire contact-resonance spectra for the lowest two flexural modes. Typically, spectra are acquired for three or more values of d at a given location on the specimen. This not only increases the number of data points, but also provides insight into the tip-sample contact.

6. Repeat steps 2-5 on the test specimen, at the same values for d. The setpoint voltages may differ slightly from those for the reference specimen.

7. Repeat steps 2-5 on the reference and test specimens in alternation, ending with the reference specimen. Perform sets of measurements several times on both specimens, in order to achieve a statistically sufficient number of data.

4 Data Analysis Methods

Data analysis consists of two distinct steps, each involving a separate model. First, the measured frequencies are related to the tip-sample interaction force by means of a model for the dynamic motion of the cantilever. Next, the interaction force—the contact stiffness—is used to determine the elastic properties of the sample through a model for the contact mechanics between the tip and the sample. Here, we present without proof the equations needed for both models. For further discussion, the reader is referred to Ref. [22]. The development here is intended to facilitate software implementation. Because the analysis models are based on analytical formulas, calculations are straightforward to implement in commercial software such as LabVIEW or IDL (ITT Visual Information Solutions, Boulder, CO).

4.1 Model for Cantilever Dynamics

Figure 4.1(a) shows the model to describe the cantilever's vibrations in free space. It is important to note that a distributed-mass model is used, not a point-mass (harmonic oscillator) model. It has been shown that the point-mass approximation does not produce accurate results under the conditions described here [31,32]. Because estimates of the tip mass are typically less than 0.5 % of the cantilever mass, it is neglected. The cantilever is modeled as an elastically isotropic beam of uniform cross section with length L, width w, thickness b, density ρ, and Young's modulus E. The tip is located at a distance $L_1 < L$ from the clamped end of the cantilever. The remaining distance to the free end of the cantilever is L', so that $L = L_1 + L'$. The flexural spring constant of the cantilever is $k_{lever} = Eb^3w/(4L_1^3)$. The frequency f_n^0 of the nth free flexural resonance is related to the wavenumber x_n^0 by

$$\left(x_n^0 L\right)^2 = 4\pi f_n^0 \frac{L^2}{b}\sqrt{\frac{3\rho}{E}} = f_n^0 \left(c_B L\right)^2 \quad . \tag{4.1}$$

$x_n^0 L$ is also a root of

$$1 + \cos x_n^0 L \cosh x_n^0 L = 0 \quad . \tag{4.2}$$

The first four roots of Eq. 4.2 are $[x_1^0 L,\ x_2^0 L,\ x_3^0 L,\ x_4^0 L]$ = [1.8751, 4.6941, 7.8548, 10.996]. Experimental values for the cantilever parameter $c_B L$ for each mode can therefore be calculated from the measured values of the free frequencies f_n^0. This approach means that cantilever properties such as L and E need not be determined directly. Equation 4.1 also shows that

$$\frac{f_n^0}{f_{n-1}^0} = \left(\frac{x_n^0 L}{x_{n-1}^0 L}\right)^2 \quad . \tag{4.3}$$

Inserting the values of $x_n^0 L$ given above into Eq. 4.3 yields the ratios listed in Table 2.1.

Fig. 4.1 Models for cantilever dynamics. (a) Tip out of contact. (b) Tip in contact. Only normal (vertical) elastic forces are considered. (c) Tip in contact, with both normal and tangential elastic forces included.

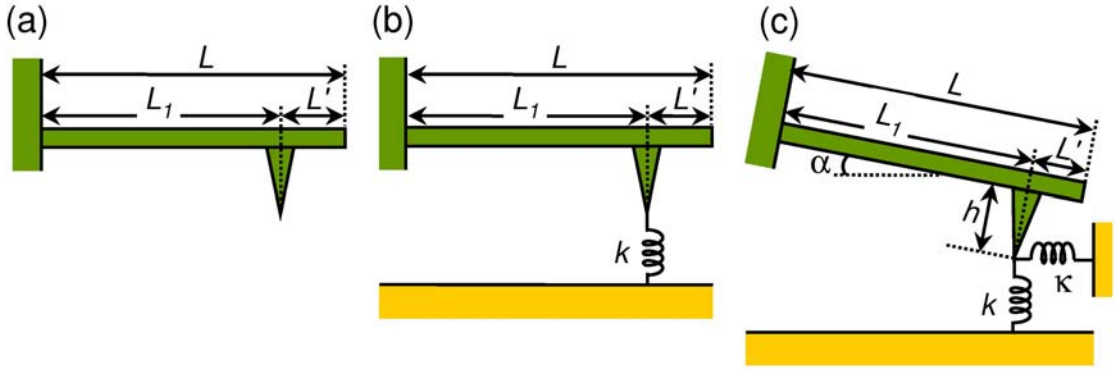

Figure 4.1(b) depicts the simplest model for cantilever dynamics if the tip is in contact. In this case, the tip-sample interaction is entirely elastic and acts in a direction normal (vertical) to the sample surface. The tip-sample interaction is represented by a spring with spring constant k, also known as the contact stiffness. By considering the dynamics of this system [32], it is found that the normalized contact stiffness k/k_{lever} is given by

$$\frac{k}{k_{lever}} \left[\left(\sin x_n L' \cosh x_n L' - \cos x_n L' \sinh x_n L'\right)\left(1 - \cos x_n L_1 \cosh x_n L_1\right) - \left(\sin x_n L_1 \cosh x_n L_1 - \cos x_n L_1 \sinh x_n L_1\right)\left(1 + \cos x_n L' \cosh x_n L'\right)\right] = \frac{2}{3}\left(x_n L_1\right)^3 \left(1 + \cos x_n L \cosh x_n L\right) \quad . \quad (4.4)$$

Here, x_n is the wavenumber of the nth flexural contact resonance. Rewriting Eq. 4.4 in terms of the relative tip position ratio $\gamma = L_1/L$ and rearranging terms, we find

$$\frac{k}{k_{lever}} = \frac{2}{3}\left(x_n L \gamma\right)^3 \frac{\left(1 + \cos x_n L \cosh x_n L\right)}{D} \quad , \quad (4.5)$$

where

$$D = \left[\sin x_n L(1-\gamma) \cosh x_n L(1-\gamma) - \cos x_n L(1-\gamma) \sinh x_n L(1-\gamma)\right]\left[1 - \cos x_n L\gamma \cosh x_n L\gamma\right] - \left[\sin x_n L\gamma \cosh x_n L\gamma - \cos x_n L\gamma \sinh x_n L\gamma\right]\left[1 + \cos x_n L(1-\gamma) \cosh x_n L(1-\gamma)\right] \quad .$$

In the data analysis, Eq. 4.5 is used to calculate k/k_{lever} for each measured contact-resonance frequency f_n. First, the values of f_n are used to calculate $x_n L$:

$$x_n L = c_B L \sqrt{f_n} = x_n^0 L \sqrt{\frac{f_n}{f_n^0}} \quad , \quad (4.6)$$

where Eq. 4.1 has been used. From the experimental values of $x_n L$, Eq. 4.5 is then used to plot k/k_{lever} as a function of the relative tip position $\gamma = L_1/L$ for each mode n. Figure 4.2 is an example of the resulting plot. The graph shows that the values of k/k_{lever} are the same for the two flexural modes at only one value of γ. This value of k/k_{lever} where the two modes intersect or "cross" is taken as the solution. An online calculator that performs this operation for $n = 1$ and 2 is available [33].

To aid the reader in developing data analysis software, Table 4.1 contains experimental values of the contact-resonance frequencies and the corresponding values of k/k_{lever} and L_1/L. It can be seen that for these data, the calculated values of $L_1/L \approx 0.97$. Direct measurement of the cantilever dimensions in SEM and optical micrographs suggests that the actual tip location $L_1/L \approx 0.91$–0.92 for this particular cantilever. Discrepancies between the calculated and measured values of L_1/L have been observed previously [24,34]. The most likely explanation is the deviation of the cantilever's actual behavior from that predicted by the idealized beam model. For instance, Fig. 2.1 reveals that the cantilever cross section near the tip end is not uniform for this type of cantilever. A mass or volume analysis of the actual cantilever shape suggests a higher value of L_1/L than that obtained from simple length analysis.

Table 4.1 Examples of experimental results. The test specimen was a <102> SnO_2 nanobelt (NB) and the reference material was <100> Si. Measurements were performed with cantilever #1 in Table 2.1. Shown are the contact-resonance frequencies f_1 and f_2 of the lowest two flexural modes versus the cantilever static deflection d. Also shown are the values of the relative tip position L_1/L for which the normalized contact stiffness k/k_{lever} is the same for both modes.

specimen	trial #	d (nm)	f_1 (kHz)	f_2 (kHz)	L_1/L	k/k_{lever}
Si <100> (reference)	1	15	732.0	1803.4	0.974	63.7
		30	734.5	1806.4	0.973	64.1
		45	737.3	1832.8	0.973	67.5
SnO_2 NB (test)	1	15	727.3	1784.2	0.976	61.3
		30	732.5	1802.8	0.974	63.7
		45	734.5	1817.8	0.973	65.5
Si <100> (reference)	2	15	735.0	1818.0	0.973	65.6
		30	737.8	1827.5	0.972	66.8
		45	739.3	1840.5	0.972	68.5

Fig. 4.2 Normalized contact stiffness k/k_{lever} as a function of the relative tip position L_1/L. Results are shown for $n = 1$ (green line) with $f_1 = 734.5$ kHz and $n = 2$ (pink line) with $f_2 = 1806.4$ kHz (see Table 4.1). The measurements were made with cantilever #1 in Table 2.1. The arrows indicate the values of k/k_{lever} and L_1/L where the two curves intersect or "cross."

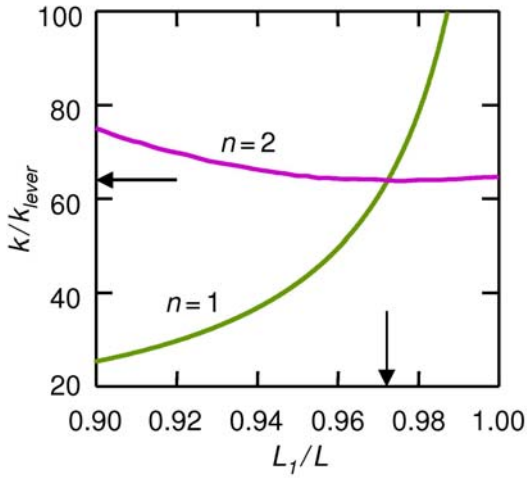

If lateral elastic forces are included, the model shown in Fig. 4.1(c) is used. The cantilever is tilted by an angle α with respect to the sample surface. The tip has height h. The elastic interaction between the tip and the sample is represented by two springs: a vertical spring with stiffness k and a horizontal (tangential) spring with stiffness κ. The

vertical contact stiffness k normalized by the flexural cantilever stiffness k_{lever} is given by [34-36] the positive root of

$$\frac{k}{k_{lever}} = \frac{-B \pm \sqrt{B^2 - 4AC}}{6A} \quad , \tag{4.7}$$

where

$$A = \left(\frac{\kappa}{k}\right)\left(\frac{h}{L_1}\right)^2 \left(1 - \cos x_n L \cosh x_n L_1\right)\left(1 + \cos x_n L' \cosh x_n L'\right) \quad ,$$

$$B = B_1 + B_2 + B_3 \quad ,$$

$$C = 2\left(x_n L_1\right)^4 \left(1 + \cos x_n L_1 \cosh x_n L\right) \quad ,$$

with

$$B_1 = \left(\frac{h}{L_1}\right)^2 \left(x_n L_1\right)^3 \left(\sin^2 \alpha + \frac{\kappa}{k}\cos^2 \alpha\right) \times$$
$$\left[\left(1 + \cos x_n L' \cosh x_n L'\right)\left(\sin x_n L_1 \cosh x_n L_1 + \cos x_n L_1 \sinh x_n L_1\right)\right. \quad ,$$
$$\left. - \left(1 - \cos x_n L_1 \cosh x_n L_1\right)\left(\sin x_n L' \cosh x_n L' + \cos x_n L' \sinh x_n L'\right)\right]$$

$$B_2 = 2\left(\frac{h}{L_1}\right)\left(x_n L_1\right)^2 \left(\frac{\kappa}{k}\cos\alpha \sin\alpha\right) \times$$
$$\left[\left(1 + \cos x_n L' \cosh x_n L'\right)\left(\sin x_n L_1 \sinh x_n L_1\right)\right. \quad ,$$
$$\left. + \left(1 - \cos x_n L_1 \cosh x_n L_1\right)\left(\sin x_n L' \sinh x_n L'\right)\right]$$

$$B_3 = \left(x_n L_1\right)\left(\cos^2 \alpha + \frac{\kappa}{k}\sin^2 \alpha\right) \times$$
$$\left[\left(1 + \cos x_n L' \cosh x_n L'\right)\left(\sin x_n L_1 \cosh x_n L_1 - \cos x_n L_1 \sinh x_n L_1\right)\right. \quad .$$
$$\left. - \left(1 - \cos x_n L_1 \cosh x_n L_1\right)\left(\sin x_n L' \cosh x_n L' - \cos x_n L' \sinh x_n L'\right)\right]$$

The inclusion of lateral forces greatly increases the number of variables involved. It is therefore desirable to use the simpler model in Fig. 4.1(b) when possible. The conditions under which this model is valid are discussed in Sect. 6. More detailed discussions of this model and its application to CR-FM analysis have been presented elsewhere [22,34,36].

Damping (inelastic or dissipative) interactions are beyond the scope of this discussion. In the model for cantilever dynamics, damping is included by means of one or more dashpots in parallel with the springs. This model is discussed in detail elsewhere [22,36]. Analysis of CR-FM data with the inclusion of damping effects has been presented [37,38]. Further work is needed to develop a practical data analysis procedure that includes damping terms.

4.2 Model for Contact Mechanics

After obtaining values for the normalized contact stiffness k/k_{lever} from the measured contact-resonance frequencies, we can use these values to determine elastic properties of the specimen. This step of the analysis requires a second model, namely one for the contact mechanics between the tip and the sample. A complete discussion of contact mechanics is given elsewhere [39]. The analysis is similar in many respects to that used to interpret instrumented (nano-) indentation data [2,28].

The key parameters of two different models for contact mechanics are shown in Fig. 4.3. The indentation moduli of the tip and the sample are M_{tip} and M_s, respectively. Figure 4.3(a) represents Hertzian contact between a hemispherical tip with radius of curvature R and a flat sample. A vertical (normal) static load F_N is applied to the tip, creating a circular contact of radius a. Figure 4.3(b) shows flat-punch contact between a flat tip and a flat sample. In this case, the contact area is constant with F_N and is determined by the tip diameter $2a$. For both cases, the vertical contact stiffness k between the tip and the sample is given by

$$k = 2aE^* \quad , \tag{4.8}$$

where E^* is the reduced elastic modulus for the tip-sample system:

$$\frac{1}{E^*} = \frac{1}{M_{tip}} + \frac{1}{M_s} \quad . \tag{4.9}$$

For elastically isotropic materials, the indentation or plane strain modulus $M = E/(1-\nu^2)$, where E is Young's modulus E and ν is Poisson's ratio. Then

$$\frac{1}{E^*} = \frac{1-\nu_{tip}^2}{E_{tip}} + \frac{1-\nu_s^2}{E_s} \quad . \tag{4.10}$$

To determine E^* from Eq. 4.8, it is necessary to know the contact radius a. For a flat indenter ("flat punch"), a is constant. For Hertzian contact, a is given by

$$a = \sqrt[3]{\frac{3RF_N}{4E^*}} \quad . \tag{4.11}$$

Fig. 4.3 Models for (a) Hertzian contact between a hemispherical tip and a flat sample and (b) flat-punch contact between a flat tip and a flat sample.

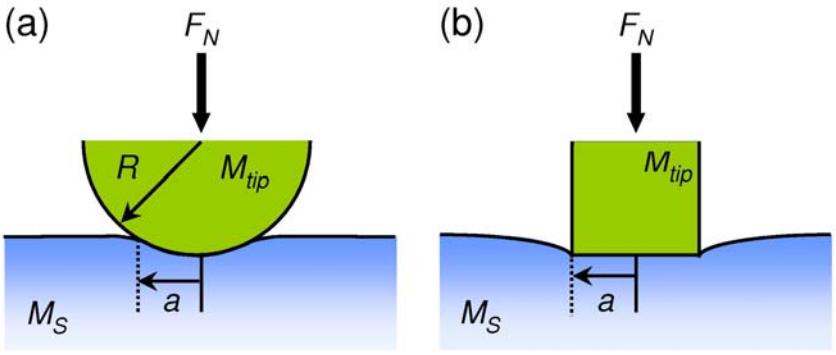

In principle, one could measure a directly (for a flat punch), or determine experimental values for R and F_N and calculate a. Equation 4.8 or 4.11 could then be used to determine E^* and hence M. In practice, a referencing or comparison approach is used [24,29] in which measurements are performed on the test (subscript s) and reference (subscript ref) samples at the same values of F_N. The approach assumes that the values of M_{ref} and thus E^*_{ref} are known. Then it can be shown [29] that

$$E^* = E^*_{ref}\left(\frac{k_s}{k_{ref}}\right)^m = E^*_{ref}\left(\frac{\dfrac{k_s}{k_{lever}}}{\dfrac{k_{ref}}{k_{lever}}}\right)^m , \qquad (4.12)$$

where $m = 3/2$ for Hertzian contact and $m = 1$ for a flat punch. From the values of E^* obtained by Eq. 4.12 with the experimental values of k_s/k_{lever} and k_{ref}/k_{lever} , the modulus M of the sample can be calculated with Eq. 4.9. As discussed in Sect. 7, the true shape of the tip is usually intermediate between a hemisphere and a flat [40]. Thus $m = 3/2$ and $m = 1$ represent upper and lower limits on M. Values for E^* obtained with this approach for the data in Table 4.1 are shown in Table 4.2. Also included are the values of the sample modulus M calculated from E^* assuming Hertzian and flat-punch contact.

Table 4.2 Results of contact-mechanics analysis for the data in Table 4.1. The contact-stiffness ratio k_{test}/k_{ref} is given for each combination of test and reference measurements. The corresponding values of the reduced elastic modulus E^* and the indentation modulus M of the test specimen are shown, assuming either Hertzian (m=3/2) or flat-punch (m=1) contact. The values $M_{tip} = M_{ref} = 165.1$ GPa were used.

data pair	***d* (nm)**	k_{test}/k_{ref}	***E** (GPa) *m* = 1**	***M* (GPa) *m* = 1**	***E** (GPa) *m* = 3/2**	***M* (GPa) *m* = 3/2**
test 1/ ref 1	15	0.963	79.5	153.4	78.1	148.0
	30	0.993	82.0	162.9	81.7	161.8
	45	0.971	80.2	155.9	79.0	151.6
test 1/ ref 2	15	0.936	77.2	145.1	74.7	136.4
	30	0.953	78.7	150.2	76.7	143.5
	45	0.956	78.9	151.3	77.2	145.0

The referencing approach invented by Rabe and coworkers [29] represents an important measurement innovation for CR-FM methods. Accurate determination of properties such as R, a, and F_N are extremely difficult due to their small size. Moreover, the Si tip often changes size and shape over the course of the measurements. This means that direct characterization approaches such as the "area function" method used in nanoindentation [28] are fraught with error for AFM tips. The referencing method avoids these issues. It also avoids direct measurement of the cantilever spring constant k_{lever}, which can be difficult to do with sufficient accuracy (see, for instance, Ref. [41]). As

long as the laser alignment on the cantilever remains constant, a given cantilever deflection always yields the same applied static force F_N. The only assumption made about the tip shape is that of axial symmetry.

5 Survey of Contact Resonance Force Microscopy Measurements

Table 5.1 contains a survey of modulus measurements reported in the literature [24,26,29,30,37,42-56]. All of the listed experiments used CR-FM methods, although some [50,55] used a data analysis approach different from that described above. The body of work has grown significantly in recent years. The table indicates the wide scope of materials that have been examined. In some cases, "model" materials such as bulk single crystals or blanket thin films were investigated in order to better understand certain measurement issues. In other cases, the spatial resolution of CR-FM made it possible to examine micro- to nanoscale features such as piezoelectric domains and grain boundaries. Some measurements were made with the point-by-point approach described above, while others involved quantitative images (modulus maps).

Also shown in Table 5.1 are values for the approximate measurement uncertainty σ for each experiment. The values were estimated from information given in the references. In many cases, σ was determined by scatter in the individual measurements and not by an uncertainty analysis. Strictly speaking, these values correspond to measurement precision or repeatability, not accuracy. Previous discussions of accuracy [44,48] gave a conservative estimate of 40 %. It can be seen from Table 5.1, however, that many experiments achieve better measurement uncertainty—as low as ±1 % in some cases. There are many factors that account for the variation in σ from experiment to experiment, for instance, sample smoothness or uniformity, the amount of tip wear during measurements, and assumptions made in the data analysis concerning tip shape. It should be noted that the lowest values of σ have usually been achieved in imaging experiments [30,46,51], which yield a very large number of measurements for statistical analysis.

Other work besides that listed in Table 5.1 has been performed to characterize materials with CR-FM methods. Martensitic phase transformations in nickel-titanium alloys were studied by measuring the cantilever vibration amplitude near resonance as a function of temperature [57]. The dependence of contact-resonance frequencies on the thickness of tungsten and polymer films was examined [58]. Measurements of contact-resonance frequencies were used to determine Young's modulus of polypyrrole polymer nanotubes [59]. Contact-resonance measurements and images were used along with other methods to characterize nanocrystalline chromium nitride films [60].

So far, we have discussed measurements of *flexural* contact-resonance frequencies to determine the elastic modulus *M*. Other work has utilized *torsional* cantilever modes to obtain additional information. Various CR-FM methods have been used to investigate the tribological properties of materials (see, for instance, Refs. [16,61-65]). Detailed reviews of this topic can be found elsewhere [66,67]. It was also recently shown that by measuring the contact-resonance frequencies of both flexural and torsional modes, shear elastic properties such as Poisson's ratio or shear modulus could be determined independently from Young's modulus or *M* [34].

Table 5.1 Survey of experimental results for the indentation modulus *M* measured by CR-FM. The first two columns give the material and the type of specimen, including the thickness *t* if appropriate. Values in the "σ" column represent the estimated measurement uncertainty.

material	specimen	*M* (GPa)	σ (%)	comments	ref.
Al	film, t = 1.09 μm	54-81	± 3-5	compared to SAWS & NI	42
Au CaF_2 MgF_2 Si	film, t = 300 nm <100> single crystals	102-104 121-123 164-180 169-181	± 1-5	dual reference method; values depend on which reference specimens used	30
$BaTiO_3$	<100> grain	(a) 75-350 (b) 318 ± 30 (c) 220 ± 50	± 9-23	values for (a) modulus map; (b) *a*-domains; (c) *c*-domains	43
clay (dickite)	*c*-axis particles	6.8 ± 2.7	± 15-40	multiple reference materials	44
diamond-like carbon (DLC)	films, t = 5 nm t = 20 nm	107 ± 12 210 ± 63	± 10-30	"preliminary values"	45
DLC	thin film	35-300	± 4	values from modulus map	46
epoxy/silica	nanocomposite plate	7-80	N/A	modulus maps	47
nanocrystalline (nc) ferrites	films, t = 200 nm	70-190	± 8-10	*M vs*. oxidation temperature	48
glass (FSG)	film, t = 3.08 μm	57-64	± 5	humidity effects observed	37
GaAs InP	<100> single crystals	112-125 88-96	± 1-15	values depend on model and cantilever used	49
lead zirconate titanate (PZT)	plate, t = 7 mm	137 ± 18 147 ± 19	± 13	inhomogeneous sample; values for two positions	29
PZT	plate, t = 300 μm	(a) 132 (b) 116	N/A	values (a) within domain, (b) at domain boundary	50
Nb	film, t = 280 nm	86-127	± 1-18	values depend on models, cantilever, reference(s)	24,42
Nb	film, t = 200 nm	119 ± 7	± 6	modulus map	51
nc Ni	films, t = 53 nm t = 204 nm t = 772 nm	223 ± 28 220 ± 19 210 ± 26	± 9-13	nanocrystalline effects; consistent with NI and SAWS results	52,53
Si	<111> single crystal	171-174	± 1	compared to NI	29
SnO_2 nanobelt	t = 44 nm	154 ± 18	± 9-12	agrees with UFM results	26
nc SnSe	film, t = 20 nm	20-50	N/A	modulus map	54
WC-Co	cermet plate	730 ± 50 (WC) 260 ± 40 (Co)	± 7-15	analysis by fit to full spectrum; no reference	55
ZnO nanowires	26-134 nm diameter	115-218	± 7-13	size effects observed	56

6 Theoretical Principles for Optimizing Experiments

As discussed above, CR-FM involves two separate models: one for the cantilever dynamics, and one for the tip-sample contact mechanics. To achieve good measurements, the experimental parameters must be chosen to satisfy *both* models simultaneously. In this section, we address the key issues of each model that are involved in optimizing these parameters.

6.1 Cantilever Dynamics: Which Modes?

In the procedure described above, the frequencies of the two lowest-order flexural resonances are measured. Why are these particular modes used? The answer is found by considering the relation between the contact-resonance frequency f_n and the normalized contact stiffness k/k_{lever}. We will call this relation the "response curve." Figure 6.1 shows f_n versus k/k_{lever} for the first three flexural modes (n = 1, 2, 3). The values of f_n are normalized to the first free flexural frequency f_1^0. Such curves are calculated with Eq. 4.5, Eq. 4.7, or with an online calculator [33]. The figure shows that the response is qualitatively similar for each flexural mode. When k/k_{lever} is relatively small, f_n remains close to its free-space value f_n^0. As k/k_{lever} increases, the change in frequency for a given change in contact stiffness gradually increases. Figure 6.1(a) shows that the relative tip position L_1/L affects the overall shape of the response curve.

The region of the response curve with the highest sensitivity is where the frequency change is the greatest (i.e., with the largest slope or derivative). In this region, small changes in contact stiffness produce measurable changes in the contact-resonance frequency. It can be seen from Fig. 6.1 that this region occurs at higher values of k/k_{lever} as the mode number n increases. To ensure accurate measurements, experimental parameters should be chosen to maximize the sensitivity of at least one mode. When k/k_{lever} increases beyond the region of highest sensitivity for a given mode, the mode approaches a "pinned" state, where even relatively large changes in contact stiffness result in only small frequency shifts. Here, the contact-resonance frequency of the nth mode approaches the free-space frequency of the (n+1)th mode. Experimental conditions should be chosen to avoid mode pinning. Not only is this the least sensitive part of the response curve, but in addition measurements made under pinned conditions could be misleading. Measurements made at different static forces F_N will yield very similar values of f_n and thus very similar values of k/k_{lever}. This could lead to the incorrect conclusion that the tip shape is flat.

In addition, lateral effects become increasingly significant as the tip approaches a pinned state [68]. This can be seen in Fig. 6.1(b), which compares the response curve for normal forces alone (solid lines) to that for normal and lateral forces combined (dashed lines). The difference between the two curves for each mode increases with k/k_{lever}. Operating under conditions of high sensitivity therefore has the added benefit that the simpler (normal-forces only) model for data analysis is valid.

More insight into mode sensitivity can be gained from Fig. 6.2. Like Fig. 6.1, Fig. 6.2(a) shows how f_n varies with k/k_{lever}. Figure 6.2(b) shows the sensitivity S of each mode as a function of contact stiffness. S is defined as the derivative of f_n/f_1^0 with respect to k/k_{lever} [69]. Analytical expressions for S for the flexural and torsional modes of cantilevers with both uniform and nonuniform cross sections have been published

elsewhere [70]. Other theoretical work that includes lateral and damping forces in the calculation of S has been published [71,72]. The values of S in Fig. 6.2(b) were calculated numerically from the curves in Fig. 6.2(a). The circles indicate the values of k/k_{lever} at which S is a maximum for each mode, while the thick lines show where S is at least 80 % of the maximum value. (There is no thick line or circle shown for $n = 1$ because the region of greatest sensitivity occurs for $k/k_{lever} < 1$.) Figure 6.2(b) clearly shows that the absolute mode sensitivity is greatest for $n = 1$ and decreases as n increases. This leads to the generalization that the lowest-order modes possible should be used. The figure also indicates that the value of k/k_{lever} at which S is a maximum increases with increasing n.

Fig. 6.1 Normalized contact-resonance frequency f_n/f_1^0 *vs.* normalized contact stiffness k/k_{lever} for the three lowest-order flexural modes (n = 1, 2, 3). The curves in (a) were calculated assuming normal forces only for $L_1/L = 1.0$ (solid lines) and $L_1/L = 0.97$ (dashed lines). In (b), the solid lines indicate the calculated response for $L_1/L = 0.97$ assuming normal forces only. The dashed lines were calculated including both normal and lateral forces with $L_1/L = 0.97$, $\alpha = 11°$, $h/L_1 = 0.05$, and $\kappa/k = 0.9$.

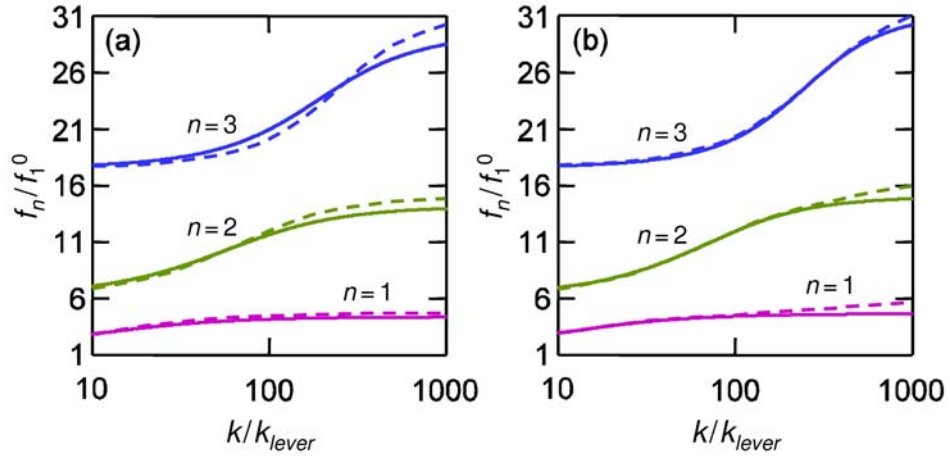

The information in graphs such as these help to establish rough guidelines for mode selection. The values used in Fig. 6.2 for the parameters L_1/L, κ/k, α, and h/L_1 are representative of typical experimental conditions. With these values, we calculate that adding lateral forces changes k/k_{lever} by approximately 5 % or less for the following conditions: for $n = 1$, $k/k_{lever} < 40$; for $n = 2$, $k/k_{lever} < 200$; for $n = 3$, $120 \le k/k_{lever} \le 600$. The most sensitive range of k/k_{lever} (80 % or more of maximum) is approximately as follows: for $n = 1$, $k/k_{lever} < 1$; $n = 2$, $0 \le k/k_{lever} \le 40$; and for $n = 3$, $30 \le k/k_{lever} \le 210$. In many experiments in the literature, k/k_{lever} ranges from approximately 50 to 100. From a sensitivity perspective, the second and third flexural modes seem the best choice for these measurements. Lateral effects are also more significant for the first mode than for the third mode in this range of k/k_{lever}. However, from a practical standpoint, the third mode is usually more difficult (if not impossible) to detect than the first mode. The absolute sensitivity of the first and third modes is also approximately the same for this range of k/k_{lever}. These facts may explain why the first and second modes have typically been used in experiments on stiff materials. It is important to recognize that the guidelines will change somewhat depending on the values of L_1/L, κ/k, α, and h/L_1 used. Readers are therefore encouraged to perform their own calculations.

Fig. 6.2 (a) Normalized contact-resonance frequency f_n/f_1^0 as a function of normalized contact stiffness k/k_{lever} for n = 1, 2, and 3. The curves were calculated including both normal and lateral forces with L_1/L = 0.97, α = 11°, h/L_1 = 0.05, and κ/k = 0.9. (b) Sensitivity S as a function of normalized contact stiffness k/k_{lever} for n = 1, 2, and 3. The circles indicate the point of maximum sensitivity for each mode. The thick lines indicate where S is at least 80 % of its maximum value. The region of maximum sensitivity for n = 1 occurs for $k/k_{lever} < 1$.

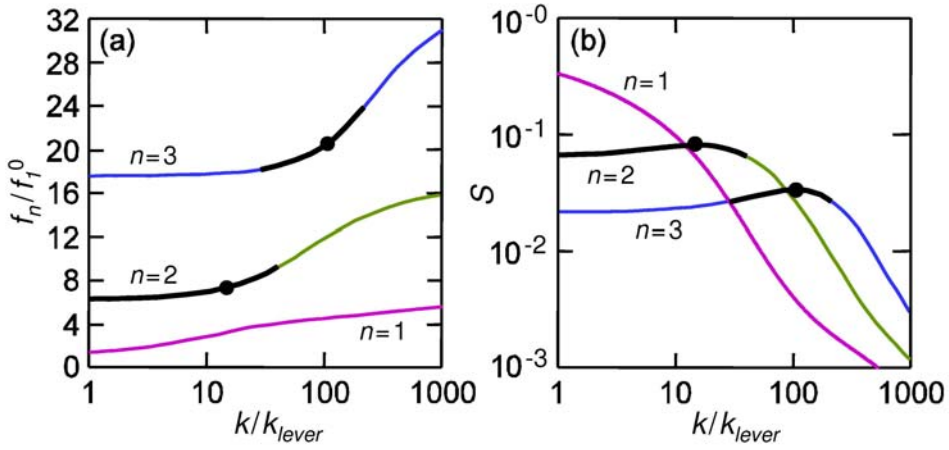

The effect of including lateral forces in the data analysis is further illustrated in Fig. 6.3, which shows the normalized contact stiffness k/k_{lever} versus relative tip position L_1/L for the three lowest-order flexural modes. The curves in Fig. 6.3 were calculated with contact-resonance frequency data from Table 4.1. If only normal forces are included (solid lines), the different mode pairs cross at different values of k/k_{lever} and L_1/L. Data analysis with this approach will yield a greater measurement uncertainty, because the variation in the crossing-point value of k/k_{lever} for different mode pairs will result in a larger scatter in M. If lateral effects are included (dashed lines), it is possible for all three modes to converge at a single value of k/k_{lever}. (The value of L_1/L also converges, and in this case increases to a value somewhat closer to that estimated from measurements of the cantilever's dimensions.) It might be possible to exploit this convergence effect to experimentally determine κ/k or h/L_1. For the data given here, the values of k/k_{lever} for the first and third modes change more than those for the second mode when lateral effects are included. This conclusion can also be reached from a detailed inspection of response curves like those in Figs. 6.1(b). However, it is the value of k/k_{lever} at which the mode pairs cross that is important. The figure shows that the crossing-point value of k/k_{lever} is virtually the same for the mode pairs n = 1,2 and n = 2,3 whether lateral effects are included or not. Because k/k_{lever} changes much more for the mode combination n = 1,3 when lateral forces are included, measurements with this pair are less reliable than with either mode pair n = 1,2 or n = 2,3 in this case.

Fig. 6.3 Normalized contact stiffness k/k_{lever} as a function of relative tip position L_1/L for data obtained with cantilever #1 in Table 2.1. The results are shown for the measured values f_1 = 734.5 kHz, f_2 = 1806.4 kHz, and f_3 = 3226.0 kHz for the contact-resonance frequencies of the three lowest flexural modes. The solid lines were calculated assuming vertical forces only, while the dashed lines include both normal and lateral forces with $\alpha = 11°$, $h/L_1 = 0.03$, and $\kappa/k = 0.9$.

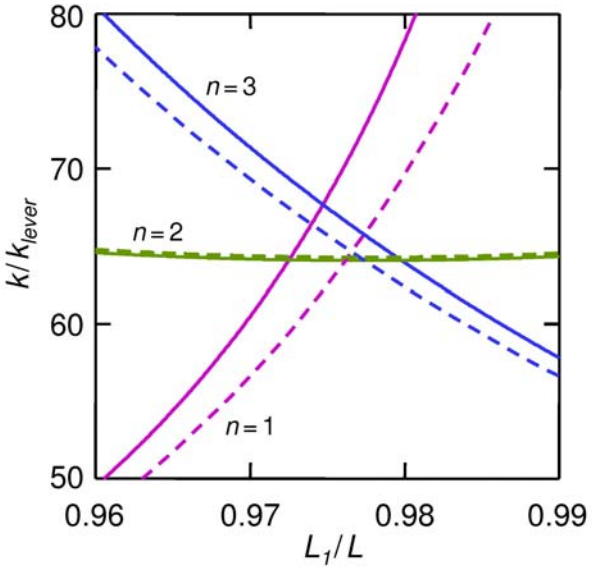

6.2 Contact Mechanics: What Forces?

Section 6.1 shows that conditions are optimized for certain values of k/k_{lever}. How do we select the experimental parameters to ensure these values? To do so, one must understand and correctly apply the principles of contact mechanics. Here, the discussion is limited to Hertzian contact mechanics. The corresponding discussion for flat-punch contact is simpler because the contact area does not depend on force.

The cantilever spring constant k_{lever} directly affects the ratio k/k_{lever}, but it also influences the contact stiffness k through the applied force F_N. F_N is determined by k_{lever} and the static cantilever deflection d through $F_N = k_{lever}d$. For Hertzian contact, the relationship between k and F_N is found by combining Eqs. 4.8 and 4.11:

$$k = 2aE^* = 2E^*\left[\sqrt[3]{\frac{3RF_N}{4E^*}}\right] = \sqrt[3]{6E^{*2}RF_N} \quad . \tag{6.1}$$

Further considerations affect the choice of k_{lever} and F_N. F_N must be sufficiently greater than any adhesion forces present to ensure that an elastic model for contact mechanics is valid. Moreover, the applied force determines the stress field in the sample, which determines the volume of the sample that is measured. For this discussion, it is simpler to work in terms of the contact radius a. Equation 4.11 gives the relation between a and F_N. For Hertzian contact, the compressional stress σ_z directly beneath the indenter as a function of depth z into the sample is given by [39]

$$\sigma_z = p_0\left(1+\frac{z^2}{a^2}\right)^{-1} \quad , \tag{6.2}$$

where $p_0 = 3F_N/(2\pi a^2)$ is the maximum stress applied at the surface, $z = 0$. Equation 6.2 shows that σ_z decreases rapidly with increasing distance into the sample. For $z = 3a$, $\sigma_z = 0.1p_0$; thus for $z > 3a$, σ_z is considered negligible. This leads to the general guideline that measurements probe to a depth $z \sim 3a$ [39,73].

This guideline can be used to tailor the experimental conditions to a particular sample. For instance, measurements of bulk specimens or relatively thick films should probe sufficiently deeply to minimize the contribution of any damage or contamination layers. Such layers are typically a few to several nanometers thick. For $k_{lever} \sim 40$ N/m on materials with $M > 50$ GPa, the probed depth exceeds 10 nm at an applied force of a few hundred nanonewtons, so this condition is easily met. In other cases, it may be important to minimize the measurement depth. In thin-film systems, for instance, the properties of the substrate will affect the measurements if the stress field extends too deeply. By keeping the applied force, and thus the depth of measurement sensitivity, sufficiently low, the film properties can be measured directly without the added complication of incorporating substrate effects in the data analysis. For nanocrystalline nickel films on silicon, a film only ~50 nm thick was directly measured with CR-FM methods [53]. Utilizing this effect to determine film thickness has also been investigated [58,74].

Fig. 6.4 Experimental values of the indentation modulus M as a function of applied static force F_N for a nanocrystalline Ni film ~15 nm thick on a <001> Si substrate. The dashed lines show the values of M for <111> Ni and <100> Si. The error bars represent the standard deviations of six separate measurements.

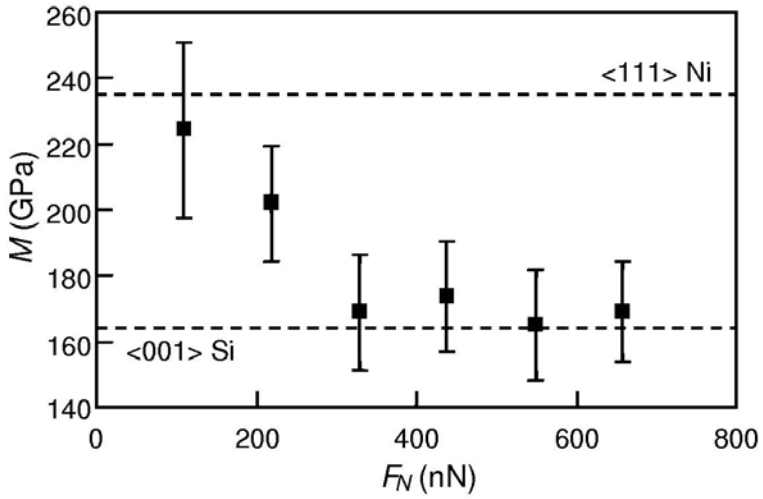

Figure 6.4 provides an example of depth effects. CR-FM experiments were performed on a sample containing a nanocrystalline nickel (Ni) film ~15 nm thick on a <001> Si substrate. The reference sample was a single crystal of <001> Ni with indentation modulus $M_{Ni} = 219$ GPa. Contact-resonance spectra were acquired at values of the static cantilever deflection $d = 10$, 20, 30, 40, 50 and 60 nm. With a cantilever spring constant $k_{lever} = 11 \pm 1$ N/m, the corresponding range of applied static force F_N was

approximately 110 nN to 660 nN. It can be seen in Fig. 6.4 that the measured value of M depends on F_N. At low applied forces, the stress field does not significantly penetrate into the Si substrate, and the values of M are similar to those measured in thicker nanocrystalline Ni films (~200-230 GPa) [53]. As the applied force increases, the stress field extends further into the substrate, and the measured response depends on the properties of both the Ni film and the Si substrate. At the highest values of F_N, the volume of material probed in the measurement consists more of the substrate than of the thin film. The response is therefore dominated by the properties of the substrate, and the measured values of M approach that of <001> Si (165 GPa). The cantilever used in these experiments was more compliant than those typically used (k_{lever} ~ 40 N/m). In the case of stiffer cantilevers, even very low deflections result in forces that are too high to sense only the properties of the film. Cantilevers with even lower values of k_{lever} could also be used to ensure suitable values of F_N. In that case, it might be necessary to utilize higher-order resonant modes to minimize lateral effects and maximize sensitivity.

The contact radius a also determines the lateral extent of the measurement sensitivity. At $z = 0$, the radial tensile stress σ_r as a function of distance r from axis of the indenter is given by [39]

$$\sigma_r = p_0\left(1-2\nu^2\right)\frac{a^2}{3r^2} \quad (r > a) \quad , \tag{6.3}$$

where ν is Poisson's ratio. For $\nu \sim 0.2$ to 0.3, σ_r falls to 10 % of its maximum value at $r \sim 1.1a$ to $1.4a$. The lateral spatial resolution is approximately twice this value, or $\sim 2a$ to $3a$, and not simply a. Thus, a balance must be maintained between achieving sufficient depth of penetration and high lateral spatial resolution. For the representative values $F_N = 1$ μN, $R = 25$ nm, and $E^* = 82.5$ GPa, we obtain $a = 6.1$ nm. Thus $3a \approx 20$ nm is a conservative estimate of both lateral and depth resolution.

6.3 An Example

The following example illustrates the principles involved in selecting experimental conditions. A sample of interest has an indentation modulus $M = 80$ GPa. Using Eq. 4.9 and assuming $M_{tip} = 165$ GPa for the <100> Si tip, we find $E^* = 54$ GPa. The radius R of the cantilever tip typically ranges from less than 10 nm (new) to approximately 50 nm (used) [40]. To probe to a depth $z \approx 3a = 10$ nm, $F_N \approx 200$ nN to 500 nN from Eq. 4.11. With these values of E^*, R, and F_N, from Eq. 4.12 we obtain $k \approx 400$ N/m to 800 N/m at the minimum load. At a maximum load of 2 μN, $k \approx 600$ N/m to 1200 N/m. For $k_{lever} = 40$ N/m, this means that $k/k_{lever} \approx 10$ to 30. For these values of k/k_{lever}, modes $n = 1$ and $n = 2$ are relatively sensitive and have minimal lateral effects. Therefore, this combination of k_{lever}, F_N, and d is a suitable choice for this specimen. Note that for $k_{lever} = 1$ N/m, deflections of $d = 200$ nm and greater would be needed to achieve $3a \approx 10$ nm. Some AFM instruments do not permit such large values of d. This is one reason why relatively stiff cantilevers are often used.

The referencing approach described in Sec. 4.2 avoids the need to determine absolute values of k_{lever} and F_N . The approach presents a distinct practical advantage, because accurate measurements of k_{lever} and AFM forces remain a challenge [14,41]. However, this discussion shows that the values of k_{lever} and F_N critically affect the

experimental conditions. Without direct measurements of k_{lever}, it is possible only to estimate properties such as F_N and a. Therefore, calculations such as the ones in the previous paragraph can only estimate k/k_{lever}. The actual values of k/k_{lever} may also differ from those calculated for other reasons. For instance, the actual contact mechanics are likely to differ from Hertzian behavior. It is advisable to compare the values of k/k_{lever} obtained in the first few measurements to the predicted values. The operating conditions, particularly F_N, can then be adjusted to enhance the response.

7 Practical Issues for Optimizing Experiments

The previous sections have discussed how some of the underlying theoretical principles affect measurement sensitivity. There are also some purely practical issues that must be considered when choosing the experimental conditions. In this section, we discuss some of these issues.

7.1 Exciting and Detecting the Cantilever's Resonant Modes

In the method described above, the resonant modes of the cantilever are excited by a separate actuator (transducer) mounted beneath the specimen. One might wonder why this additional transducer is used, when almost all AFM instruments contain a built-in actuator. Intended for use in intermittent-contact mode, this actuator is located in the cantilever holder and excites vibrations from the clamped end of the cantilever. If the electrical drive signal to the actuator can be externally controlled, CR-FM measurements can be performed with this "internal" actuator instead of an "external" transducer. This approach may be useful in certain applications, for instance if the sample is curved or otherwise prohibits access from below.

Figure 7.1 compares spectra obtained with an internal actuator and an external transducer. Figures 7.1(a) and (c) show the spectra of the first and second free resonances, while Figs. 7.1(b) and (d) contain the spectra of the corresponding contact resonances. All of the contact-resonance spectra were acquired without changing the contact between the tip and the sample. Although the free-resonance spectra appear similar, the contact resonances obtained by the different excitation means are significantly different. Spectra obtained with the internal actuator contain background signals and extraneous peaks that hinder identification of the contact-resonance frequencies. These signals may be due to resonant modes of the actuator itself, or else the silicon plate on which the cantilever is fabricated [23]. Figure 7.1 also shows that the frequency response of the internal actuator may not be adequate to sufficiently excite the higher-order resonant modes. Because results depend strongly on the specific AFM instrument used, general conclusions should not be drawn from the spectra in Fig. 7.1.

Alternatively, a custom actuator can implemented to excite the cantilever resonances. This has usually been accomplished by attaching the actuator to the base of the cantilever [19,75]. However, cantilevers with integral actuation elements have recently been developed [76]. Excitation by means of a transducer beneath the sample was first developed as the AFAM method by Rabe and coworkers [22,31]. Excitation with an actuator at the clamped end of the cantilever was first developed as the UAFM method by Yamanaka and coworkers [19,75]. Mathematical analyses of both systems have been published [22,77]. The analyses show that as long as damping terms are small,

the contact-resonance peaks occur at the same frequencies regardless of excitation method. However, the amplitude of the cantilever vibration and other details of the response spectrum differs between methods.

Fig. 7.1 Spectra excited by an "external" transducer mounted beneath the sample (solid lines) and by the AFM's "internal" piezoelectric element in the cantilever holder (dotted lines). The sample was a glass slide. Spectra for the first and second free resonances are shown in (a) and (c), while the corresponding contact-resonance spectra are shown in (b) and (d), respectively.

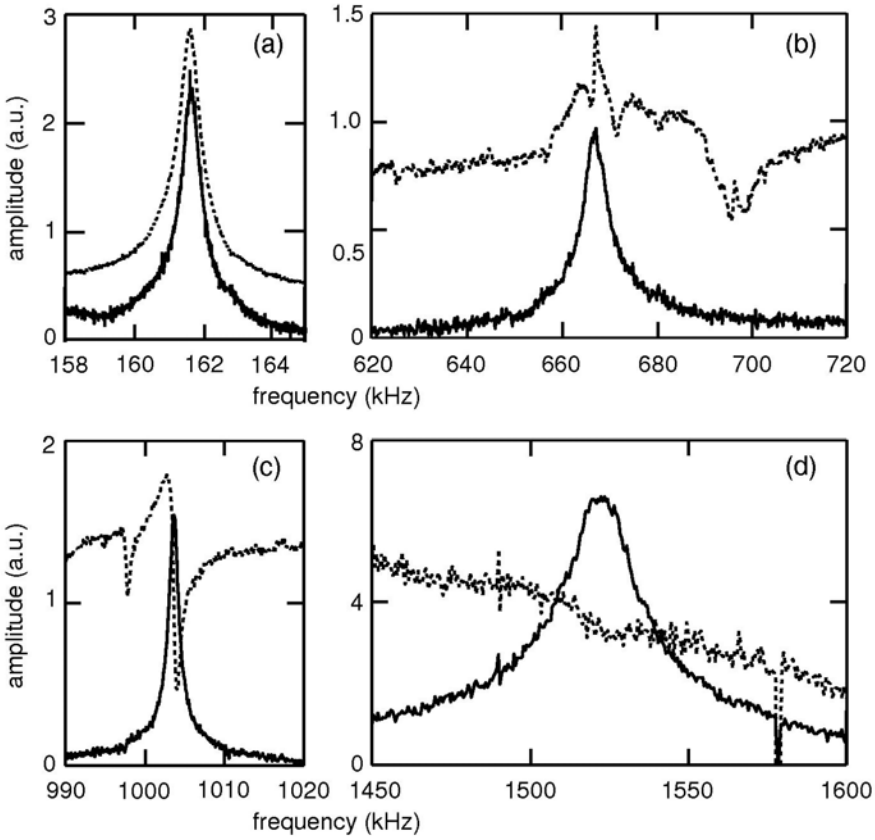

Practical issues also affect the ability to experimentally detect the contact resonances. In particular, the size and relative position of the laser spot can affect the detected signal amplitude [31,78,79]. This effect can be better understood by considering the vibration amplitude versus position on the cantilever that is predicted for a given mode and given contact stiffness [31]. Such considerations suggest that for optimum detection sensitivity, the best position of the laser spot is not always at the very end of the cantilever. The exact behavior depends strongly on the specific experimental conditions. Under typical experimental conditions, our experience has generally been that the amplitude of the first mode drops relatively sharply as the laser is moved away from the end of the cantilever towards its clamped base. The amplitude of the second mode drops more gradually with distance, and can sometimes actually increase as the spot is moved away from the tip end towards the clamped base. In this way, it may be possible to adjust the relative amplitudes of the detected modes. The finite diameter of the laser spot (~50

μm) further complicates matters, especially for the higher-order modes. If the laser spot is sufficiently large compared to the wavelength of a given mode, the detected signal may be virtually zero in some positions. The lateral (side-to-side) position of the laser spot may also change the detected signal. Poor lateral positioning is one possible reason that spectra can sometimes appear asymmetrical.

7.2 Tip Shape and Tip Wear

Measurements are also affected by practical issues concerning the tip shape. One issue is the nonideal shape of the real cantilever tip and how it affects the nanoscale contact mechanics. As seen in SEM images such as those shown in Figs. 2.1, Fig. 7.2(a), and 7.3(a), the cantilever tip usually does not conform to an idealized shape such as a hemisphere. Several studies have been performed to better understand the effect of the true tip shape on measurements [40,45,49,80].

In our studies of tip shape [40], CR-FM experiments were performed with several cantilevers with similar characteristics. The tips of the cantilevers were imaged with high-resolution SEM techniques before and after each set of experiments. The SEM images were used to determine directly the tip shape and dimensions such as the tip radius R. These values were then compared to those inferred from the CR-FM data by means of contact-mechanics models. The results showed that none of the standard contact-mechanics models describe the actual behavior of the tips. Figure 7.2(b) shows the measured contact stiffness k as a function of static applied force F_N for three cantilevers. Although the dimensions and free frequencies of the cantilevers were virtually identical, the dependence of k on F_N was different in each case. Based on the results from ten different cantilevers, we found that the force dependence was best described by $k \propto F_N^{\beta}$. The exponent β was varied to allow for tip shapes intermediate between a flat punch (β = 0) and a hemisphere (β = 1/3).

Fig. 7.2 (a) SEM image of a new cantilever tip. The cantilever was similar to cantilever #1 in Table 2.1. (b) Vertical contact stiffness k as a function of the applied static load F_N for three cantilevers obtained from the same manufacturer at the same time. The dotted lines indicate fits to the form $k \propto F_N^{\beta}$, where β = 0 corresponds to a flat tip and β = 1/3 corresponds to a hemispherical tip.

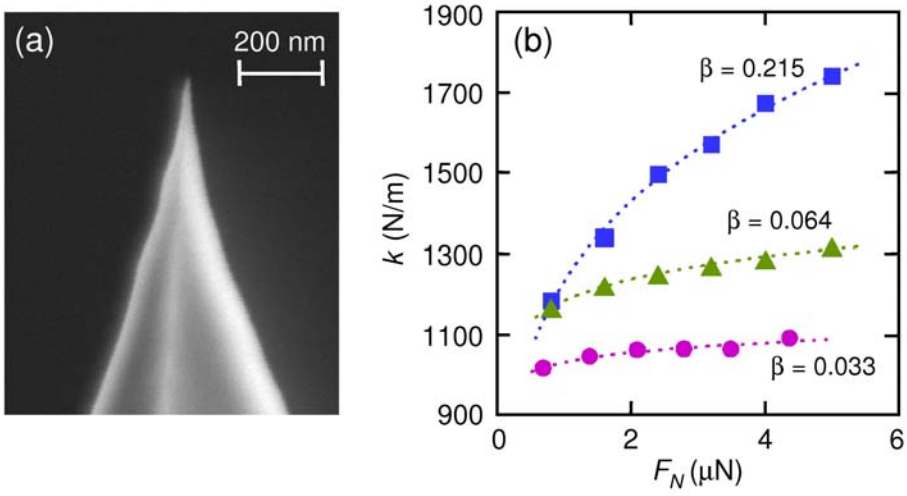

Another practical issue is tip wear—changes in tip shape and size during use. When used in contact at loads up to a few micronewtons, sharp tips such as those shown in Figs. 2, 7.2(a), and 7.3(a) gradually grow blunter, suddenly break, or plastically deform [40,45,49]. Gradual tip wear is illustrated in Fig. 7.3(b), which shows values for k/k_{lever} measured in alternation on fused silica ($M \approx 75$ GPa) and an aluminum film ($M \approx 79$ GPa). Although the applied load was kept the same throughout the measurements, it can be seen that k/k_{lever} gradually increased due to tip wear. Tip wear means that the radius R increases, causing the contact radius a and thus k to increase. However, each subsequent measurement of k/k_{lever} for the aluminum film was greater than the previous one for fused silica (with one exception). Therefore, the referencing approach described above will yield accurate values for M despite gradual tip wear [29]. This motivates the practice of measuring the reference specimen before and after each measurement on the unknown specimen. Figure 7.3(b) shows that k/k_{lever} approaches an equilibrium value after a few dozen measurements. The exact behavior depends on the specific materials involved as well as the load history. Such results suggest that it might be desirable to "wear in" tips before use. Although this procedure could degrade the spatial resolution slightly, it could yield more reproducible results and lead to less data scatter. Systematic studies to investigate methodologies for such a "tip wear procedure" have not been reported.

Fig. 7.3 Examples of tip wear in CR-FM experiments. (a) SEM image of a sharp tip in side view. (b) Measured values of the normalized contact stiffness k/k_{lever} for fused silica (SiO_2, triangles) and an aluminum film (Al, squares). The film was approximately 1 μm thick on a sapphire substrate. The first measurement corresponds to a new tip similar to the one shown in (a). The measurements were made at a static deflection d = 30 nm, corresponding to an applied static force $F_N \approx 1.2$ μN. (c) SEM image of a deliberately shaped tip in side view. (d) Normalized contact stiffness k/k_{lever} for SiO_2 (triangles) and an Al film (squares) using the tip shown in (c). The first measurement corresponds to a new tip. The measurements were made at a static deflection d = 35 nm.

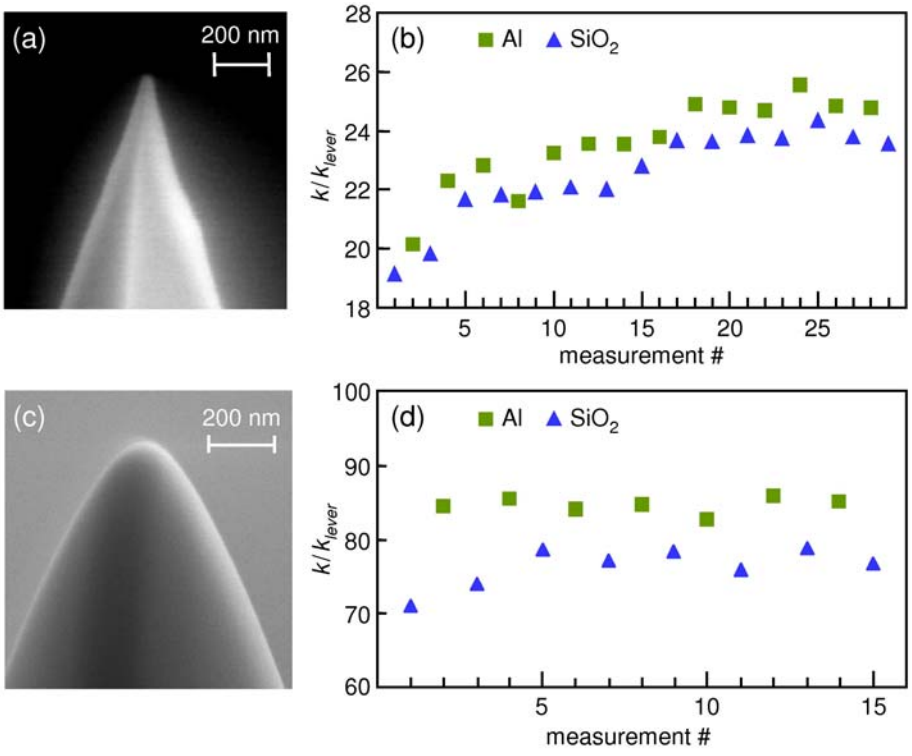

Results such as these could lead to improved measurement procedures. The experimental uncertainty in the modulus M is often inflated in order to accommodate the range of values that results from assuming $m = 1$ and $m = 3/2$ in Eq. 4.12. Developing a tip characterization procedure might allow a more exact value of m to be used for each set of measurements, and thus reduce uncertainty. The procedure could be based on the dependence of k on F_N [40,80], or might take a different approach.

A possible solution to tip wear, breakage, and deformation is the use of tips with a larger radius of curvature R. Figure 7.3 shows the results of CR-FM experiments to investigate this idea. As seen in Fig. 7.3(c), the cantilever had a deliberately rounded tip (Nanosensors, Neuchâtel, Switzerland). The nominal value of R ranged between 90 nm (end view) and 160 nm (side view). Figure 7.3(d) shows that the normalized contact stiffness k/k_{lever} rapidly approaches an equilibrium value, indicating very little wear. Similar results have been observed by another group [81]. Although further measurements are needed, these initial results suggest that larger tips may be useful for quantitative modulus measurements, if a decrease in spatial resolution can be tolerated.

A final issue involving practical considerations is the choice of reference specimen. It has been found that the best quantitative results are obtained if the indentation modulus M_{ref} of the reference material is similar to the modulus M_s of the unknown specimen. One reason is possible uncertainty in the value M_{tip} used in Eq. 4.9 for the modulus of the tip [30]. This can be better understood by rewriting the equations in Sec. 4.2 as

$$\frac{1}{M_s} = \left(\frac{k_{ref}}{k_s}\right)^m \left(\frac{1}{M_{ref}}\right) + \frac{1}{M_{tip}}\left[\left(\frac{k_{ref}}{k_s}\right)^m - 1\right] . \qquad (7.1)$$

If the unknown and reference materials have similar modulus, $k_{ref} / k_s \approx 1$. This means that the quantity in square brackets in Eq. 7.1 is small, and the impact of inaccuracy in the value of M_{tip} is minimized. The use of two reference materials has also been demonstrated as a way to overcome the difficulty of accurately knowing M_{tip} [22,24,30].

Another consideration in choosing reference materials is the presence of any surface layers such as oxides or adsorbed water. These layers cause the real system to deviate from the idealized one used in the data analysis. An oxide layer means that the sample is a two-layer system instead of a uniform half space. Capillary layers due to adsorbed water create significant adhesive forces, so that pure elastic contact cannot be assumed. Surface roughness is also a consideration. Smooth samples provide greater uniformity in the contact conditions across the surface, and therefore reduce data scatter.

8 Imaging with Contact Resonance Force Microscopy

So far in this chapter, we have described how CR-FM is used for measurements at a fixed sample position. However, the two-dimensional scanning capability of the AFM instrument makes it ideal for creating images of the spatial distribution in properties. One reason for the growing demand for spatial visualization of properties is the increasing integration of multiple materials on micro- and nanometer scales. The cause of failure in such systems is often a localized variation in properties. Because measurements of "average" sample properties are simply not sufficient in such cases, images are required.

Initially, images obtained by CR-FM methods gave only qualitative information about elastic properties [12,20,75,82]. Such "amplitude images" are nonetheless useful in many applications and are straightforward to acquire experimentally. In this approach, the excitation frequency is set close to that of the contact resonance for a particular mode. The output amplitude signal of the lock-in amplifier is connected to an auxiliary input channel of the AFM instrument and is used for image acquisition. The resulting image thus contains the relative amplitude of the cantilever vibration at the excitation frequency for each position on the sample. The contrast in amplitude images may be enhanced or suppressed by the choice of excitation frequency [29]. At relatively low frequencies, the cantilever vibration amplitude will be higher for regions with lower elastic modulus. More compliant regions will therefore appear brighter. Increasing the excitation frequency so that it is close to the contact-resonance frequency of stiffer sample components decreases the vibration amplitude of more compliant regions. Hence, stiffer regions will appear brighter. In this way, one can observe a reversal or "inversion" in image contrast by changing the excitation frequency [11].

Examples of amplitude imaging are shown in Fig. 8.1. The sample contained a blanket film of an organosilicate glass (denoted SiOC) approximately 280 nm thick. Copper (Cu) lines were deposited into trenches created in the SiOC blanket film. The sample was etched briefly in a hydrofluoric acid solution to remove any protective surface layers. The topography image of Fig. 8.1(a) reveals that the sample is very flat, with height variations less than ~5 nm to 10 nm. Figures 8.1(b) and (c) show amplitude images acquired at two different frequencies. Small features inside the Cu lines can be seen. These are most likely due to shifts in the contact area that arise from small topographical features (*e.g.*, pores, polishing effects). In addition to the SiOC film and the Cu lines, bright regions can be seen at the SiOC/Cu interfaces. This feature corresponds to a thin barrier layer deposited on the sidewall of the trenches, and is not obvious in the topography image. In Fig. 8.1(b), the SiOC regions of the image are brighter than the Cu regions. However, the Cu regions are brighter in the image in Fig. 8.1(c), which was acquired at a higher excitation frequency. This information suggests that the contact-resonance frequency of the Cu regions is generally higher than that of the SiOC regions. Because higher contact-resonance frequencies imply greater elastic modulus, it can be inferred that the modulus of the Cu lines is greater than that of the SiOC film.

Fig. 8.1 Example of CR-FM or AFAM amplitude imaging. The sample contained copper (Cu) lines in an organosilicate glass (SiOC) film. (a) Topography. The image was acquired in contact mode, at the same time as the image in (c). (b) Amplitude image of the cantilever vibration for an excitation frequency f = 550 kHz. (c) Amplitude image at f = 630 kHz. Images were acquired with a cantilever with lowest free-space frequency f_1^0 = 151.3 kHz.

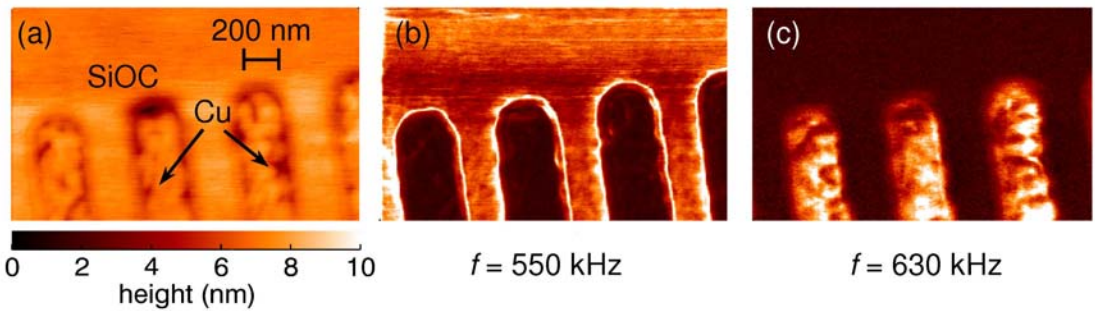

Figure 8.1 shows that components of different elastic stiffness are easily identified by amplitude imaging. However, the figure also illustrates the difficulties involved in trying to evaluate the relative stiffness of different sample components. Instead, quantitative imaging or *mapping* of nanoscale elastic properties is ultimately desired. Quantitative imaging requires detecting the frequency of the contact-resonance peak at each position as the tip moves across the sample. A single such contact-resonance-frequency image can provide more information than an entire series of amplitude images. However, if the sample components differ greatly in their elastic properties, the contact-resonance frequency will vary significantly across the sample, making detection more difficult. Several solutions to this challenge have been demonstrated [17,30,43,46,83-85]. Typically, there is a tradeoff between the imaging speed and the amount of custom hardware and software required.

We have also developed techniques for nanomechanical mapping with CR-FM [51,86,87]. Our approach differs conceptually from other implementations, in that the starting frequency of the frequency sweep window is continuously adjusted to track the contact-resonance peak. In this way, a high-resolution spectrum is acquired with a minimum number of data points, even if the frequency of the peak shifts significantly throughout the image. Other approaches that lack feedback must perform a frequency sweep at every pixel over the same relatively wide range that encompasses all possible peaks. Our approach also utilizes a digital signal processor (DSP) architecture. One advantage of a DSP approach is that it facilitates future upgrades, because changes are made in software instead of hardware.

A schematic of the "frequency-tracking" apparatus is shown in Fig. 8.2. The electronics are explained in greater detail elsewhere [87]. An adjustable-amplitude, swept-frequency sinusoidal voltage is applied to the piezoelectric actuator beneath the specimen. As the cantilever is swept through its resonant frequency by the actuator, the photodiode detects the cantilever's vibration amplitude and sends this signal to the DSP circuit. The circuit converts the signal to a voltage proportional to the root-mean-square (rms) amplitude of vibration and digitizes it with an analog-to-digital (A/D) converter. As each sweep completes, the circuit constructs a complete resonance curve. It finds the peak in the resonance curve and uses this information in a feedback-control loop. The control loop adjusts a voltage-controlled oscillator (VCO) to tune the center frequency of vibration to maintain the cantilever response curve centered on resonance. The control voltage is also routed to an input port of the AFM instrument for image acquisition. Each pixel in the resulting image thus contains a value proportional to the peak (resonant) frequency at that position. A frequency range can be specified in order to exclude all but the cantilever mode of interest. A total of 128 data points are acquired for each resonance curve. At 48 kilosamples per second, the system acquires the full cantilever resonance curve 375 times per second. The AFM scan speed must be adjusted to ensure that several spectrum sweeps are made at each image position. For scan lengths up to several micrometers, an image with 256×256 pixels is usually acquired in less than 25 min.

Fig. 8.2 Schematic of experimental apparatus for contact-resonance-frequency imaging.

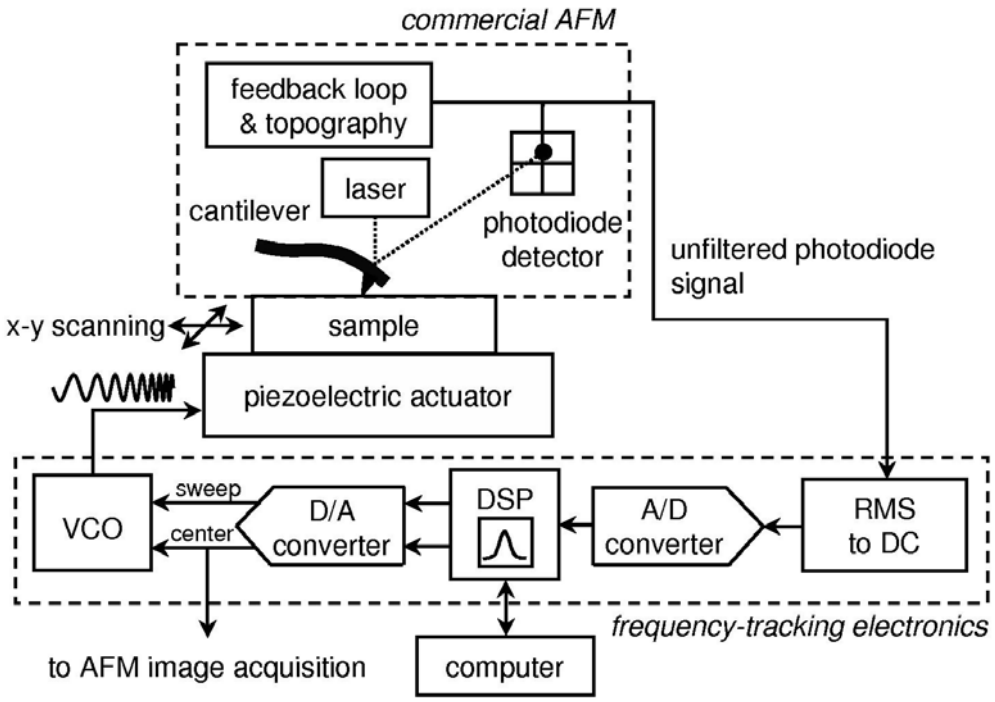

An example of quantitative imaging with our frequency-tracking electronics is shown in Fig. 8.3. The images correspond to the same region of the SiOC/Cu structure as that shown in Fig. 8.1. The topography image in Fig. 8.3(a) shows the SiOC blanket film and the slightly recessed (less than 5 nm) Cu lines. The contact-resonance-frequency images for the two lowest flexural modes of the cantilever are shown in Figs. 8.3(b) and (c), respectively. The frequency images reveal directly that the contact-resonance frequency in the Cu regions is higher than that in the SiOC regions.

Figure 8.3(d) shows a map of the normalized contact stiffness k/k_{lever} calculated from the frequency images in Figs. 8.3(b) and (c). The image was calculated on a pixel-by-pixel basis with the analysis approach described above for point measurements. Depending on the application, it may be sufficient to evaluate the contact-stiffness map alone. In other cases, a map of the indentation modulus M may be needed. Calculating a modulus map from the contact-stiffness image involves the same models and assumptions used for point measurements. For instance, a specific contact-mechanics model must be chosen. Reference values of E^* and k/k_{lever} are also needed. Here, we calculated the modulus map from the contact-stiffness image with the assumption that the tip was flat. We also assumed that the mean value of E^* in the SiOC region corresponded to $M_{SiOC} = 44.3$ GPa. This value was obtained from independent point measurements directly on the SiOC film with a borosilicate glass as the reference material. The average value of k/k_{lever} in the SiOC region of the image was used as the reference value. The resulting modulus map is shown in Fig. 8.3(e). In spite of the assumptions made to obtain the map, it shows how quantitative images of M can be achieved. Other mapping results are listed in Table 5.1.

Fig. 8.3 Example of quantitative CR-FM imaging. (a) Topography. (b) and (c) Contact-resonance frequency images of the first (f_1) and second (f_2) flexural modes, respectively. (d) Normalized contact stiffness k/k_{lever} calculated from (b) and (c). (e) Map of the indentation modulus M calculated from (d), as described in the text. The free-space frequencies of the cantilever's lowest two flexural modes were f_1^0 = 151.3 kHz f_2^0 = 938.0 kHz.

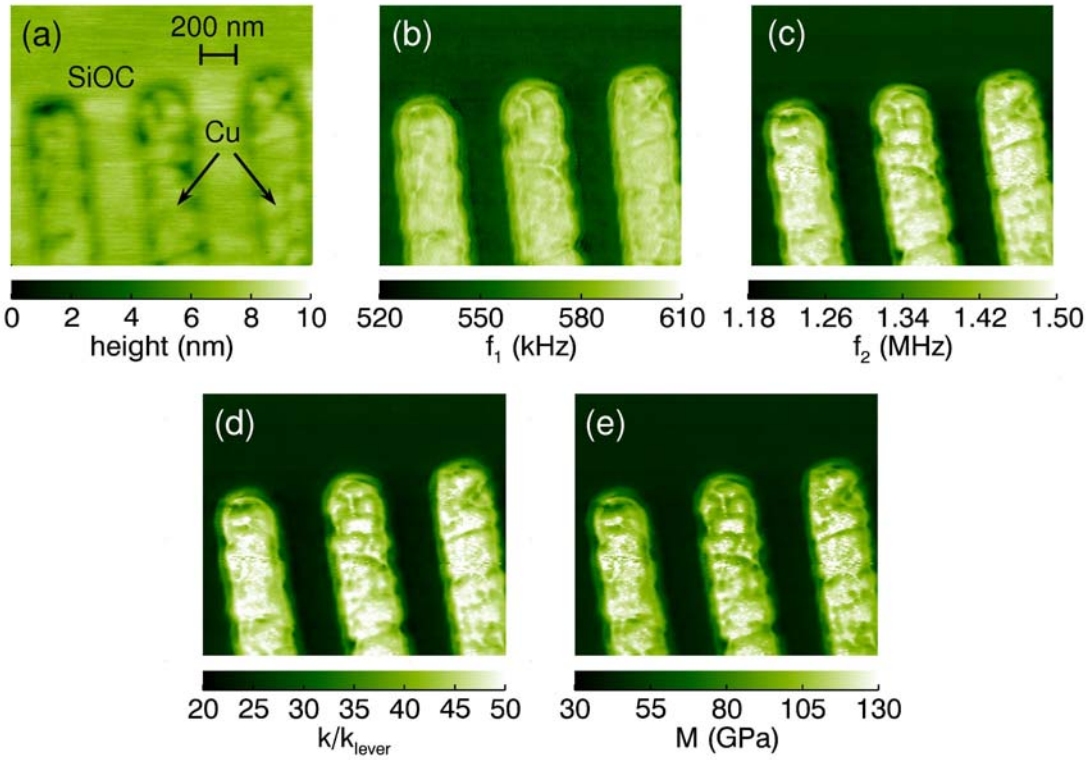

Imaging techniques might also be used to improve point measurements of M. Recently, values for M in homogeneous samples were obtained from contact-resonance-frequency images [30]. Images for the two lowest flexural modes were acquired by scanning small regions of the sample. The average frequency of each image was determined and used to calculate the contact stiffness k/k_{lever}, from which M could be calculated. An advantage of this approach is that it yields many more data points in a much shorter time than can be obtained from individual point measurements. When combined with the use of two reference materials, the measurement uncertainty of this approach (scatter in data points) was typically less than 1 %. Further evaluation of this approach is needed, for instance to establish the variability in images acquired under nominally identical conditions.

Other mechanical properties besides elastic modulus can be imaged with CR-FM methods, if they influence the contact stiffness between the tip and the sample. It was explained in Sec. 6.2 how CR-FM probes the sample properties to a depth z roughly three times that of the tip-sample contact radius a. CR-FM can thus be used to sense variations in mechanical properties beneath the surface, for example to investigate subsurface dislocations [88,89]. In other recent work, amplitude imaging was used to detect very large voids (diameter 50 μm to 500 μm) buried several hundred nanometers below the surface [90]. Cracks in buried layers have also been studied with UFM methods [91].

Another property of technological interest is the relative bonding or adhesion between a film and a substrate. To investigate the sensitivity of CR-FM to variations in film adhesion [92], we fabricated a model system of gold (Au) and titanium (Ti) films on (001) Si. Figure 8.4(a) shows a cross-sectional schematic of the sample. A rectangular grid of Ti 1 nm thick containing 5 μm × 5 μm holes (10 μm pitch) was created on Si by standard microfabrication techniques. A blanket film of Au 20 nm thick and a topcoat of Ti 2 nm thick were deposited on top of the grid. A crude scratch test was performed by lightly dragging one end of a tweezer across the sample. Optical micrographs showed that this treatment had removed the film in the scratched regions without a Ti interlayer (squares), and left the gold intact in the scratched regions containing a Ti interlayer (grid). The result confirmed our expectation that the film adhesion was much stronger in regions containing the Ti interlayer. The Ti topcoat was included merely to prevent contamination of the AFM tip by the soft Au film.

Fig. 8.4 Evaluation of film/substrate adhesion with CR-FM imaging. (a) Schematic of sample in cross section. (b) Map of the normalized contact stiffness k/k_{lever} calculated from contact-resonance-frequency images. (c) Average stiffness versus position across the center of (b).

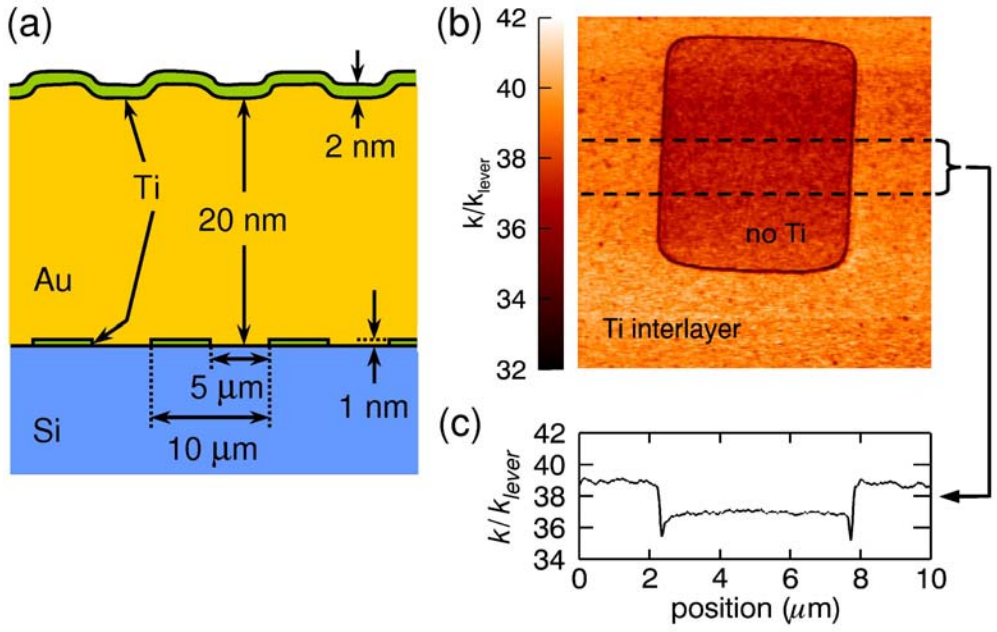

Frequency-imaging experiments were performed on the sample. A map of the normalized contact stiffness k/k_{lever} calculated from the resulting contact-resonance frequency images is shown in Fig. 8.4(b). The image shows that k/k_{lever} is lower in the region with poor adhesion (no Ti interlayer). A line scan of the average value of k/k_{lever} for 40 lines in the center of the image is shown in Fig. 8.4(c). The mean value of k/k_{lever} is 39.1 ± 0.6 in the grid regions and 37.1 ± 0.5 in the square, a difference of 5 %. Additional images acquired at different sample positions consistently showed a decrease in k/k_{lever} of 4 % to 5 % for the regions of poor adhesion that lacked a Ti interlayer.

From Eq. 4.11, we estimate that a = 6 nm to 8.5 nm for our experimental parameters. The experiments should therefore probe the film interface (z = 22 nm to 24

nm ≈ 3a). The observed results are also consistent with theoretical predictions for layered systems with disbonds [74,93]. In that work, the film/substrate system was modeled with an impedance-radiation approach that included a change in boundary conditions at the disbonded interface (i.e., zero shear stress). For a disbond in an aluminum film 20 nm thick on (001) silicon, a reduction of approximately 4 % in the contact stiffness was predicted, very similar to our results. Although the parameters used in the theoretical study differed from those in our experiments, the overall combination of conditions (film and substrate modulus, applied force, etc.) was sufficiently similar to ours that we believe a comparison is valid. These results represent progress towards quantitative imaging of adhesion, a goal with important practical implications for many thin-film devices.

9 The Road Ahead

In this chapter, we have described contact resonance force microscopy (CR-FM) methods and their use for materials characterization on the nanoscale. CR-FM experiments involve measuring the resonant frequencies of a vibrating cantilever when its tip is in contact with a material. Models for the cantilever dynamics and for the tip-sample contact mechanics are then used to relate the contact-resonance frequencies to the near-surface elastic properties. The basic physical principles have been discussed, as well as the experimental apparatus and current best practices for measurements. Principles to optimize experimental conditions were explained and used to motivate the best practices. Some of these principles are of a more theoretical nature, such as the signal response curve. Others are more practical, such as tip shape and wear. Finally, methods for qualitative and quantitative nanomechanical imaging with CR-FM were described. We hope that the discussion stimulates readers to envision applications of CR-FM in their own research.

Although CR-FM methods are sufficiently mature to serve as a useful tool, there is still room for improvement. Extensions or refinements to the basic technique could not only yield better measurements, but could also lead to exciting new applications. Here, we briefly discuss some of the key directions for future work. The ideas can be grouped into three broad themes: improving precision and accuracy, reducing measurement time, and adapting techniques to new material systems.

Measurement accuracy and precision might be improved by using custom-fabricated cantilevers, instead of relying on commercially available ones. For example, optimal sensitivity in combined torsional- and flexural-mode experiments were hampered by the range of available cantilevers [34]. Accuracy could also be improved by fabricating cantilevers whose response more closely matches that predicted by the data analysis model. For instance, a nonuniform or nonrectangular cross section may shift the spacing of the free frequencies. Vibrational behavior can also be affected by asymmetries in the cantilever beam [94], or by the clamping conditions of the cantilever holder [23]. In one case, the resulting spurious modes were reduced by patterning the backside of the cantilever substrate [95]. A more radical approach involves redesigning the cantilever geometry. Examples of this approach in other AFM applications include cantilevers with higher-order modes that occur at an exact integer multiple of the fundamental mode [96], and cantilevers whose free frequencies are adjusted to accommodate the bandwidth of the AFM photodiode [97].

Instead of designing a new cantilever, accuracy might be improved with a better model to predict the dynamic behavior of real cantilevers. One possibility is to replace the relatively simple analytic model with a more detailed model involving finite-element analysis (FEA). FEA models have been developed to evaluate the dynamic behavior of resonant cantilevers in free space [98] and in contact [99-101]. With a FEA approach, information about the actual geometry of the cantilever obtained from SEM or other imaging tools is easily incorporated. This feature is particularly valuable when the cantilever geometry varies significantly from a rectangular shape [100]. In spite of progress, an alternative to the existing analytical model that is suitable for practical measurements has not yet been reported.

Measurements could also be improved by a better understanding of the tip-sample contact behavior. As discussed in Sec. 7.2, an improved procedure to characterize the true tip shape could increase precision. Work to characterize tips for other AFM applications might provide insight into this issue [102-104]. Tip wear also adds to measurement uncertainty. As described above and in Ref. [105], deliberately blunted or rounded tips could address this problem. In order to maintain high spatial resolution, however, sharp yet robust tips will ultimately be needed. Tips with hard wear coatings are commercially available and seem ideally suited. In practice, however, the coatings tend to fracture [45], and can be insufficiently smooth for consistent tip-sample contact. As with cantilever geometry, it may be necessary to fabricate custom tips. Carbon-coated tips with a hemispherical shape were created in one study with promising results [106].

Future work to reduce measurement time will contain both experimental and theoretical aspects. From a practical standpoint, minimizing tip wear could reduce measurement time in addition to increasing accuracy. More robust tips might enable measurement redundancy to be minimized and the number of reference measurements to be reduced. From a theoretical standpoint, measurement time could be cut virtually in half by devising a method that requires the frequency of only one resonant mode. Currently, the frequencies of two modes are needed to determine both the normalized contact stiffness k/k_{lever} and the relative tip position L_1/L. Perhaps L_1/L could be determined in another way, for instance through an additional calibration procedure, FEA modeling, or SEM imaging. Rapid or even simultaneous measurement of multiple modes would also reduce measurement time [107]. Increased speed in imaging applications is also important. There are physical limits on the ultimate scanning speed that can be attained. However, current times of ~30 min or longer to acquire one frequency image could be reduced considerably before reaching these limits. This is area of active research not only for AFM in general [108,109], but also for CR-FM in particular [17].

Extending the range of materials and applications that can be addressed with CR-FM methods is an exciting prospect. For instance, dynamical processes could be studied if faster imaging rates were possible. Measurements on extremely thin films (~20 nm or less) also require refinements such as an analysis approach that includes the substrate properties [110]. New applications involving highly compliant materials such as polymers present other challenges, because CR-FM methods were originally developed for use on much stiffer materials. For instance, lower static forces are needed to prevent sample damage, requiring the use of cantilevers with a lower spring constant. To optimize the response of such cantilevers, measurements with higher-order mode pairs (*e.g.*, $n = 2, 3$ or $n = 3, 4$) may be needed. Analysis of low-force data is also likely to

involve inelastic or damping effects (see, for example, Ref. [39] or [111]). Such effects can arise not only from a surface capillary layer, but from the viscoelastic nature of the material itself. It may eventually be possible to quantitatively evaluate extremely compliant (M < 100 MPa) materials with CR-FM [112].

The above discussion presents a variety of measurement challenges for CR-FM methods. Successfully meeting these challenges will enable researchers to better address materials problems in emerging applications as well existing ones. The increased use and applicability of these methods will contribute to the rapid growth of nanoscale materials science. For all of these reasons, the future seems bright for CR-FM methods as a valuable tool for materials characterization.

Acknowledgements

I am grateful for the many contributions made by M. Kopycinska-Müller (now at IZFP/IAVT-TU, Dresden, Germany) to this work while at NIST from 2003 to 2006. The idea for this chapter originated from our discussions together. I also thank colleagues at NIST who contributed in many ways to this work: M. Fasolka, R. Geiss, A. Kos, E. Langlois (now at Analog Devices, Boston, Massachusetts), J. Pratt, P. Rice (now at the University of Colorado-Boulder), D. Smith, C. Stafford, and G. Stan. I value many interactions over the years with researchers from other institutes, especially with J. Turner and students (University of Nebraska-Lincoln), and W. Arnold, U. Rabe, and S. Hirsekorn (Fraunhofer Institute for Nondestructive Testing IZFP, Saarbrücken, Germany). I also value collaborations and discussions with R. Geer (University at Albany, State University of New York), B. Huey (University of Connecticut-Storrs), N. Jennett and M. Monclus (National Physical Laboratory, Teddington, UK), and M. Prasad (Colorado School of Mines, Golden). The data on SnO_2 nanobelts presented in this chapter were the result of a visit to NIST by Y. Zheng (then at the University at Albany).

References

1. http://www.nano.gov/NNI_07Budget.pdf (accessed August 2008)
2. Oliver WC, Pharr GM (1992) J Mater Res 7:1564
3. Syed Asif SA, Wahl KJ, Colton RJ, Warren OL (2001) J Appl Phys 90:1192
4. Li X, Bhushan B (2002) Mater Charact 48:11
5. Every AG (2002) Meas Sci Technol 13:R21
6. Ogi H, Tian J, Tada T, Hirao M (2003) Appl Phys Lett 83:464
7. Cretin B, Sthal F (1993) Appl Phys Lett 62:829
8. Kraft O, Volkert CA (2001) Adv Engng Mater 3:99
9. Binnig G, Quate CF, Gerber Ch (1986) Phys Rev Lett 56:930
10. Maivald P, Butt HJ, Gould SAC, Prater CB, Drake B, Gurley JA, Elings VB, Hansma PK (1991) Nanotechnology 2:103
11. Burnham NA, Kulik AJ, Gremaud G, Gallo PJ, Oulevey F (1996) J Vac Sci Technol B 14:794
12. Troyon M, Wang Z, Pastre D, Lei HN, Hazotte A (1997) Nanotechnology 8:163
13. Rosa-Zeiser A, Weilandt E, Hild S, Marti O (1997) Meas Sci Technol 8:1333
14. Cappella B, Dietler G (1999) Surface Sci Repts 34:1
15. Zhong Q, Inniss D, Kjoller K, Elings VB (1993) Surface Sci 290:L688
16. Yamanaka K, Ogiso H, Kolosov OV (1994) Appl Phys Lett 64:178
17. Huey BD (2007) Annu Rev Mater Res (2007) 37:351
18. Cuberes MT, Assender HE, Briggs GAD, Kolosov OV (2000) J Phys D: Appl Phys 33:2347
19. Yamanaka K, Nakano S (1996) Jpn J Appl Phys 35:3787
20. Rabe U, Arnold W (1994) Appl Phys Lett 64:1493
21. Dinelli F, Castell MR, Ritchie DA, Mason NJ, Briggs GAD, Kolosov OV (2000) Phil Mag A 80:2299
22. Rabe U (2006) Atomic force acoustic microscopy. In: Bushan B, Fuchs H (eds) Applied scanning probe methods vol II. Springer, Berlin Heidelberg New York, p 37
23. Rabe U, Hirsekorn S, Reinstädtler M, Sulzbach T, Lehrer C, Arnold W (2007) Nanotechnology 18:044008
24. Hurley DC, Shen K, Jennett NM, Turner JA (2003) J Appl Phys 94:2347
25. Commercial equipment and materials are identified only in order to adequately specify certain procedures. In no case does such identification imply recommendation or endorsement by the National Institute of Standards and Technology, nor does it imply that the materials or equipment identified are necessarily the best available for the purpose.
26. Zheng Y, Geer RE, Dovidenko K, Kopycinska-Müller M, Hurley DC (2006) J Appl Phys 100:124308
27. Papadakis EP (1990) The measurement of ultrasonic velocity. In: Thurston RN, Pierce AD (eds) Physical Acoustics vol XIX. Academic Press, San Diego, p 81
28. Oliver WC, Pharr GM (2004) J Mater Res 19:3

29. Rabe U, Amelio S, Kopycinska M, Hirsekorn S, Kempf M, Göken M, Arnold W (2002) Surf Interf Anal 33:65

30. Stan G, Price W (2006) Rev Sci Instr 77:103707

31. Rabe U, Janser K, Arnold W (1996) Rev Sci Instr 67:3281

32. Turner JA, Hirsekorn S, Rabe U, Arnold W (1997) J Appl Phys 82:966

33. http://em-jaturner.unl.edu/AFMcalcs.htm (accessed August 2008)

34. Hurley DC, Turner JA (2007) J Appl Phys 102:033509

35. Wright OB, Nishiguchi N (1997) Appl Phys Lett 71:626

36. Rabe U, Turner J, Arnold W (1998) Appl Phys A 66**:**S277

37. Hurley DC, Turner JA (2004) J Appl Phys 95:2403

38. Hurley DC, Kopycinska-Müller M, Julthongpiput D, Fasolka MJ (2006) Appl Surf Sci 253:1274

39. Johnson KL (1985) Contact Mechanics. Cambridge University Press, Cambridge UK

40. Kopycinska-Müller M, Geiss RH, Hurley DC (2006) Ultramicroscopy 106:466

41. Langlois ED, Shaw GA, Kramar JA, Pratt JR, Hurley DC (2007) Rev Sci Instr 78:093705

42. Hurley DC, Turner JA, Wiehn JS, Rice P (2002) In: Meyendorf N, Baaklini GY, Michel B (eds) Proc of the SPIE 4703. SPIE Publishers, Bellingham WA, p 65

43. Rabe U, Kopycinska M, Hirsekorn S, Muñoz Saldaña J, Schneider GA, Arnold W (2002) J Phys D: Appl Phys 35:2621

44. Prasad M, Kopycinska M, Rabe U, Arnold W (2002) Geophys Res Lett 29:13-1

45. Amelio S, Goldade AV, Rabe U, Scherer V, Bhusan B, Arnold W (2001) Thin Solid Films 392:75

46. Passeri D, Bettucci A, Germano M, Rossi M, Alippi A, Sessa V, Fiori A, Tamburri E, Terranova ML (2006) Appl Phys Lett 88:121910

47. Preghnella M, Pegoretti A, Migliaresi C (2006) Polymer Testing 25:443

48. Kester E, Rabe R, Presmanes L, Tailhades Ph, Arnold W (2000) J Phys Chem Solids 61:1275

49. Passeri D, Bettucci A, Germano M, Rossi M, Alippi A, Orlanducci S, Terranova ML, Ciavarella M (2005) Rev Sci Instr 76:093904

50. Tsuji T, Saito S, Fukuda K, Yamanaka K, Ogiso H, Akedo J, Kawakami K (2005) Appl Phys Lett 87**:**071909

51. Hurley DC, Kopycinska-Müller M, Kos AB, Geiss RH (2005) Meas Sci Technol 16:2167

52. Hurley DC, Geiss RH, Jennett NM, Kopycinska-Müller M, Maxwell AS, Müller J, Read DT, Wright JE (2005) J Mater Res 20:1186

53. Kopycinska-Müller M, Geiss RH, Müller J, Hurley DC (2005) Nanotechnology 16**:**703

54. Passeri D, Rossi M, Alippi A, Bettucci A, Manno D, Serra A, Filippo E, Lucci M, Davoli I (2008) Superlattices and Microstructures, in press (doi:10.1016/j.spmi.2007.10.004)

55. Dupas E, Gremaud G, Kulik A, Loubet J-L (2001) Rev Sci Instr 72:3891

56. Stan G, Ciobanu CV, Parthangal PM, Cook RF (2007) Nano Lett 7:3691

57. Oulevey F, Gremaud G, Mari D, Kulik AJ, Burnham NA, Benoit W (2000) Scripta mater 42:31

58. Crozier KB, Yaralioglu GG, Degertkin FL, Adams JD, Minne SC, Quate CF (2000) Appl Phys Lett 76:1950

59. Cuenot S, Frétigny C, Demoustier-Champagne S, Nysten B (2004) Phys Rev B 69:165410

60. Mangamma G, Mohan Kant K, Rao MSR, Kalavathy S, Kamruddin M, Dash S, Tyagi AK (2007) J Nanosci Nanotechnol 7:2176

61. Reinstädtler M, Rabe U, Scherer V, Hartmann U, Goldade A, Bhushan B, Arnold W (2003) J Appl Phys 82:2604

62. Drobek T, Stark RW, Gräber M, Heckl WM (1999) New J Phys 1:15

63. Kawagishi T, Kato A, Hoshi Y, Kawakatsu H (2002) Ultramicroscopy 91:37

64. Caron A, Rabe U, Reinstädtler M, Turner JA, Arnold W (2004) Appl Phys Lett 85:6398

65. Song Y, Bhushan B (2005) J Appl Phys 97:083533

66. Scherer V, Reinstädtler M, Arnold W (2004) Atomic force microscopy with lateral modulation. In: Bhushan B, Fuchs H, Hosaka S (eds) Applied scanning probe methods vol I. Springer, Berlin Heidelberg New York, p 75

67. Reinstädtler M, Kasai T, Rabe U, Bhushan B, Arnold W (2005) J Phys D: Appl Phys 38:R269

68. Mazeran PE, Loubet JL (1997) Trib Lett 3:125

69. Rabe U, Amelio S, Kester E, Scherer V, Hirsekorn S, Arnold W (2000) Ultrasonics 38:430

70. Turner JA, Wiehn JS (2001) Nanotechnology 12:322

71. Chang WJ (2002) Nanotechnology 13:510

72. Wu TS, Chang WJ, Hsu JC (2004) Microelectronic Engineering 71:15

73. Sthal F, Cretin B (1995) In: Jones JP (ed) Acoustical imaging vol 21. Plenum Press, New York, p 305

74. Yaralioglu GG, Degertekin FL, Crozier KB, Quate CF (2000) J Appl Phys 87:7491

75. Yamanaka K, Nakano S (1998) Appl Phys A 66**:**S313

76. Olson S, Sankaran B, Altemus B, Geer R, Castracane J, Xu B (2006) J Microlith Microfab Microsyst 5:021197

77. Burnham NA, Gremaud G, Kulik AJ, Gallo PJ, Oulevey F (1996) J Vac Sci Technol B 14:1308

78. Stark RW (2004) Rev Sci Instr 75:5053

79. Schäffer TE, Fuchs H (1995) J Appl Phys 97:083524

80. Yamanaka K, Tsuji T, Noguchi A, Koike T, Mihara T (2000) Rev Sci Instr 71:2403

81. Rabe U (2007) private communication

82. Rabe U, Scherer V, Hirsekorn S, Arnold W (1997) J Vac Sci Technol B 15:1506

83. Yamanaka K, Maruyama Y, Tsuji T, Nakamoto K (2001) Appl Phys Lett 78:1939

84. Kobayashi K, Yamada H, Matsushige K (2002) Surf Interf Anal 33:89

85. Efimov E, Saunin SA (2002) In: Proc of the scanning probe microscopy conference 2002, p 79. Available at http://ntmdt.com/publications?year=2002 (accessed August 2008)

86. Hurley DC, Kos AB, Rice P (2005) In: Kalinin SV, Goldberg B, Eng LM, Huey BD (eds) Proc of the MRS 838E. Mater Res Soc, Warrendale PA, p O8.2.1

87. Kos AB and Hurley DC (2008) Meas Sci Technol 19:015504

88. Tsuji T, Yamanaka K (2001) Nanotechnology 12:301

89. Tsuji T, Irihama H, Yamanaka K (2002) Jpn J Appl Phys 41:832

90. Striegler A, Pathuri N, Köhler B, Bendjus B (2007) In: Thompson DO, Chimenti DE (eds) AIP Conference Proceedings 894, Rev Prog QNDE 2006. AIP Publishing, Melville NY, p 1572

91. McGuigan AP, Huey BD, Briggs GAD, Kolosov OV, Tsukahara Y, Yanaka M (2002) Appl Phys Lett 80:1180

92. Hurley DC, Kopycinska-Müller M, Langlois ED, Kos AB, Barbosa N, (2006) Appl Phys Lett 89:021911

93. Sarioglu AF, Atalar A, Degertekin FL (2004) Appl Phys Lett 84:5368

94. Reinstädtler M, Rabe U, Scherer V, Turner JA, Arnold W (2003) Surf Sci 532-535:1152

95. Adams JD, York D, Whisman N (2004) Rev Sci Instr 75:2903

96. Sahin O, Yaralioglu G, Grow R, Zappe SF, Atalar A, Quate C, Solgaard O (2004) Sens Act A 114:183

97. Sadewasser S, Villanueva G, Plaza JA (2006) Rev Sci Instr 77:073703

98. Mendels DA, Lowe M, Cuenat A, Cain MG, Vallejo E, Ellis D, Mendels F (2006) J Micromech Microeng 16:1720

99. Arinero R, Lévêque G (2003) Rev Sci Instr 74:104

100. Shen K, Hurley DC, Turner JA (2004) Nanotechnology 15:1582

101. Espinoza Beltrán FJ, Scholz T, Schneider GA, Muñoz-Saldaña J, Rabe U, Arnold W (2007) In: Meyer E, Hegner M, Gerber C, Güntherodt H-J (eds) J Phys Conference Series 61, Proc ICN&T 2006. IOP Publishing, Bristol UK, p 293

102. Villarrubia JS (1996) J Vac Sci Technol B 14:1518

103. Villarrubia JS (1997) J Res Natl Inst Stand Technol 102:425

104. Itoh H, Fujimoto T, Ichimura S (2006) Rev Sci Instr 77:103704

105. Muraoka M (2005), Nanotechnology 16:542

106. Schwarz UD, Zwörner O, Köster P, Wiesendanger R (1997) J Vac Sci Technol B 15:1527

107. Jesse S, Kalinin SV, Proksch R, Baddorf AP, Rodriguez BJ (2007) Nanotechnology 18:435503

108. Humphris ADL, Miles MJ, Hobbs JK (2005) Appl Phys Lett 86:034106

109. Hansma PK, Schitter G, Fantner GE, Prater C (2006) Science 314:601

110. Batog GS, Baturin AS, Bormashov VS, Sheshin EP (2006) Tech Phys 51:1084

111. Schwarz UD (2003) J Coll Interf Sci 261:99

112. Ebert A, Tittmann BR, Du J, Scheuchenzuber W (2006) Ultrasound in Med & Biol 32:1687